Validation of mobile *in situ* measurements of dairy husbandry emissions by fusion of airborne/surface remote sensing with seasonal context from the Chino Dairy Complex[☆]

Ira Leifer [a,*], Christopher Melton [a], David M. Tratt [b], Kerry N. Buckland [b], Clement S. Chang [b], Jason Frash [a], Jeffrey L. Hall [b], Akihiko Kuze [c], Brian Leen [d], Lieven Clarisse [e], Tryg Lundquist [f], Martin Van Damme [e], Sam Vigil [f], Simon Whitburn [e], Leonid Yurganov [g]

[a] Bubbleology Research International (BRI), 1642 Elm Ave, Solvang CA 93463, United States
[b] The Aerospace Corporation, 2310 E. El Segundo Blvd., El Segundo CA 90245, United States
[c] JAXA, Tsukuba City, Ibaraki, 305-8505, Japan
[d] ABB, 3055 Orchard Drive, San Jose, CA 95134, United States
[e] Université Libre de Bruxelles (ULB), Brussels, Belgium
[f] California Polytechnic State University, San Luis Obispo, CA 93407, United States
[g] University of Maryland, Baltimore, MD, 21250, United States

A R T I C L E   I N F O

A B S T R A C T

Mobile *in situ* concentration and meteorology data were collected for the Chino Dairy Complex in the Los Angeles Basin by AMOG (AutoMObile trace Gas) Surveyor on 25 June 2015 to characterize husbandry emissions in the near and far field in convoy mode with MISTIR (Mobile Infrared Sensor for Tactical Incident Response), a mobile upwards-looking, column remote sensing spectrometer. MISTIR reference flux validated AMOG plume inversions at different information levels including multiple gases, GoogleEarth imagery, and airborne trace gas remote sensing data. Long-term (9-yr.) Infrared Atmospheric Sounding Interferometer satellite data provided spatial and trace gas temporal context.

For the Chino dairies, MISTIR-AMOG ammonia (NH_3) agreement was within 5% (15.7 versus 14.9 Gg yr^{-1}, respectively) using all information. Methane (CH_4) emissions were 30 Gg yr^{-1} for a 45,200 herd size, indicating that Chino emission factors are greater than previously reported.

Single dairy inversions were much less successful. AMOG-MISTIR agreement was 57% due to wind heterogeneity from downwind structures in these near-field measurements and emissions unsteadiness. AMOG CH_4, NH_3, and CO_2 emissions were 91, 209, and 8200 Mg yr^{-1}, implying 2480, 1870, and 1720 head using published emission factors. Plumes fingerprinting identified likely sources including manure storage, cowsheds, and a structure with likely natural gas combustion.

NH_3 downwind of Chino showed a seasonal variation of a factor of ten, three times larger than literature suggests. Chino husbandry practices and trends in herd size and production were reviewed and unlikely to add seasonality. Higher emission seasonality was proposed as legacy soil emissions, the results of a century of husbandry, supported by airborne remote sensing data showing widespread emissions from neighborhoods that were dairies 15 years prior, and AMOG and MISTIR observations. Seasonal variations provide insights into the implications of global climate change and must be considered when comparing surveys from different seasons.

© 2018 Published by Elsevier Ltd.

1. Introduction

1.1. Husbandry and poultry/waste systems

The environmental footprint of animal food production is

increasing due to increasing animal population and intensification of animal farming practices driven by human wealth, population growth, and shifting diets. Globally, cattle, swine, and chicken populations have increased from 0.9, 0.4, and 3.9 billion animals in 1961 to 1.5, 1.0, and 21 billion in 2014, respectively (FAO, 2016). This has implications for air and water quality and human health. For example, total greenhouse gas (GHG) emissions from all livestock in 2006 was 14.5% of all anthropogenic GHG emissions based on a carbon dioxide (CO_2) equivalent (FAO, 2016). These emissions arise from the animals, from waste management, and from farming infrastructure, with large variations depending on practices (Casey et al., 2006). Beyond CO_2 and Methane (CH_4) emissions, ammonia (NH_3) emissions play a key role in fine aerosol formation thereby affecting the global radiative balance (Paulot and Jacob, 2014).

Emissions also include trace gases, termed odorants, which comprise a vast range of trace gases. For example, Schiffman et al. (2001) identified 331 different inorganic and volatile organic compounds (VOCs) from a swine facility. The most significant trace gas is hydrogen sulfide (H_2S), which can cause health problems to workers and animals (Andriamanohiarisoamanana et al., 2017). Other important sulfur gases include mercaptans and disulfides (Casey et al., 2006).

Farm-scale emission measurements provide information that single animal emission studies cannot. Emissions from animals, waste, and infrastructure are affected by waste management practices (feed composition, manure cleaning, solids separation, storage practices, etc.), the farm microenvironment (humidity, feedlot versus pasture albedo, nocturnal lighting, etc.), and emissions upstream and downstream from farms (Hristov et al., 2013). As a feed composition example, increased dietary protein leads to decreased CH_4 but increased NH_3 and N_2O emissions (Sarkwa et al., 2016). Emissions can be characterized as a per animal emission factor, or as an emission intensity − per unit mass of animal product.

Approaches have included direct concentration measurements combined with ventilation rates (best for enclosed structures), ambient sampling with micrometeorology measurements and trajectory inversion calculations, and the use of a tracer gas to determine transport and dispersion (Phillips et al., 2000). Flux chambers can be applied to lagoons and manured surfaces but do not incorporate the impact of wind-driven air-water or air-soil exchange. Remote sensing shows great potential for some trace gas emissions, particularly, NH_3 and CH_4 (Leifer et al., 2016b); however, is unavailable for most low concentration husbandry trace gases.

Micrometeorology challenges include spatially-separated emission sources (barns, corrals, waste lagoons, etc.), ensuring sensors are downwind, the effect of structures and other obstacles on wind measurements, and accounting for shifting winds and time-varying emissions (Phillips et al., 2000). Despite these near-field challenges, health and environmental impacts are strongest in the near field, making it an important area for measurements.

Far-field measurements can suffer from intervening sources (White et al., 1976), boundary layer dynamics, including capping at some height (Leifer et al., 2013; Sasakawa et al., 2010), and chemical transformations for short-lived gases.

1.2. Study motivation and approach

Animal husbandry is an important GHG source (EPA, 2017; FAO, 2016) that arises from localized sources (dairies, feedlots, and farms) with widely varying emission factors that are highly dependent on practices and the immediate (seasonally-varying) environment. This heterogeneity manifests on a wide range of scales, from regional to facility to sub-facility, challenging assessment by fixed analyzer measurements or reductionist animal studies that cannot capture real world practices.

Integrated satellite and airborne remote sensing and mobile analytical laboratory measurements provide new and powerful tools to address these spatial and temporal multi-scale challenges. The latter is based on recent technological improvements including the development of fast, ultra-sensitive, stable Cavity Enhanced Absorption Spectroscopy (CEAS) analyzers (Leen et al., 2013).

In this study, we combine mobile remote sensing data with mobile *in situ* data and airborne remote sensing data to understand better the applicability and limitations of Gaussian plume inversion models. Additionally, we evaluate the limitations of annualizing campaign data by evaluating long-term satellite trace gas observations and meteorology data. Our analysis follows the pathway of increasing information − inversions are conducted with minimal information, to which additional information is added. Additional information can include additional *in situ* gas data, remote sensing data, airborne remote sensing trace gas data, and mobile remote sensing trace gas data.

Our focus is the Chino Dairy Complex in the Los Angeles Basin. The complex is the strongest NH_3 source in the basin as well as an important source of GHG and other husbandry trace gases. Most husbandry trace gases are at concentrations too low to be observed by current satellite and airborne remote sensing technology. Thus, scaling a retrievable gas with a strong signature, such as NH_3, with measured *in situ* ratios can allow remote sensing to estimate other trace gas emissions for comparison with, for example, health epidemiological studies.

1.3. Ammonia

NH_3 is an important husbandry emission and is the most abundant form of atmospheric gas-phase reduced nitrogen (Heald et al., 2012). Anthropogenic sources (38 Tg yr^{-1}) now overwhelm natural contributions (9−12.5 Tg yr^{-1}) to the global nitrogen cycle (Paulot et al., 2015). Agriculture is the primary anthropogenic NH_3 source (Aneja et al., 2000), although vehicle exhaust emissions can dominate in urban areas (Carslaw and Rhys-Tyler, 2013). NH_3 ecosystem implications, including eutrophication, arise from excess nitrogen input into sensitive ecosystems (Galloway et al., 2008). In coastal areas, 1−40% of total nitrogen input can arise from dry deposition (Howarth, 2008). During 2008, top NH_3 emitting countries were China, India, the US, and Brazil at 11, 4.4, 3.6, and 2.7 Tg yr^{-1}, respectively, nearly doubling since 1970 (European Commission, 2016). Strongest growth was for China, India, and Brazil, weaker growth for the US, stability in Europe, and some decrease in Africa.

Regional-scale data are needed to validate regional scale emissions inventories. For example, currently the EDGAR (Emission Database for Global Atmospheric Research) NH_3 emissions inventory database (v4.2) relies on European studies (Gilliland et al., 2003) even though husbandry practices differ between the U.S. and Europe. Globally, EDGAR attributes 58% to agricultural soil emissions (fertilizer), 21% to animal wastes, and 16% from fires (European Commission, 2009). Global husbandry NH_3 emissions likely will increase for several reasons. Firstly, dairy production and non-cattle livestock are expected to increase in the U.S. (Wescott and Trostle, 2007) and also globally. And secondly, production is becoming more intensive, particularly in the tropics (Galloway et al., 2008; Tilman et al., 2002).

Satellite observations are critical to identifying seasonal and inter-annual emission trends on regional and larger scales. Satellite NH_3 data products are available for several instruments including IASI - Infrared Atmospheric Sounding Interferometer (Clarisse et al., 2009), AIRS - Atmospheric InfraRed Sounder (Warner et al., 2016), CrIS - Cross-track Infrared Sounder (Dammers et al., 2017), and TES

- Tropospheric Emission Spectrometer (Shephard et al., 2011), with potential for other high-resolution Fourier Transform Infrared (FTIR) instruments such as GOSAT - Greenhouse gases Observing SATellite (Kuze et al., 2009).

NH_3 lifetime estimates vary from 1 h (Baek et al., 2004) to 5 days (Pinder et al., 2008) with loss from dry (or wet) deposition and by gas-to-particle conversion, e.g., the formation of NH_4^+ salt aerosols in the presence of sulfur dioxide (SO_2) or nitric acid from NO_X oxidation (Pinder et al., 2008). This conversion is bidirectional with partitioning depending on temperature, humidity, and NO_X and SO_X availability (Dawson et al., 2007).

Fertilizer NH_3 application and therefore emissions are highly seasonal (Hertel et al., 2011). Whereas fertilizer applications contributes to a springtime maximum, husbandry related emissions introduce a mid-late-summer peak (Paulot et al., 2014). For example, Gilliland et al. (2003) found an increase of ~80% for U.S. emissions between January and July, while Warner et al. (2016) found an increase of ~150% for the northern hemisphere based on long-term AIRS data. Seasonality of husbandry NH_3 emissions likely arises from the timing of manure and fertilizer application to fields and from seasonal temperature trends because volatilization from animal wastes is temperature dependent.

Husbandry NH_3 emissions arise when urea in urine is mixed with urease in feces that converts the urea into an unstable NH_3-NH_4 complex (Powell et al., 2008). This process often begins immediately upon excretion in barns where urine and feces are mixed on floors and corral ground where there also is long-term urease build up (Braam et al., 1997), but is much less efficient on open pastures. Braam et al. (1997) found that the decomposition rate of NH_3 release increases exponentially above 10 °C. One factor underlying these emissions is inefficiency in animal uptake of feed protein-nitrogen and from providing the animals with excess protein-nitrogen (Bussink and Oenema, 1998). Higher dietary crude protein increases milk production, thus economic pressures to increase production tend to increase NH_3 emissions (Reynolds and Kristensen, 2008). The importance of excess feed to NH_3 emissions was illustrated by Bussink and Oenema (1998) who found higher NH_3 emissions in cooler spring compared to warmer fall, which they attributed to higher springtime nitrogen dietary input. They also found 10–20% lower nocturnal emissions when animal activity is less. NH_3 emissions from urine are strongly correlated with animal activity, generally following the feeding schedule and varying by a factor of 3 over a day (Ngwabie et al., 2011).

NH_3 volatilization increases with manure temperature, acidity, and NH_4^+ concentration, as well as with wind speed and turbulence over the manure. In a metastudy, Bougouin et al. (2016) found barn NH_3 emissions increased with outside temperature, T, as $60 + 2.67T$ ($g\ cow^{-1}\ d^{-1}$) with no effect from wind speed. Whereas urine NH_3 is efficiently volatilized (4–41%), volatilization of NH_3 in feces is less efficient (1–13%) (Bussink and Oenema, 1998). Bedding material also can play a role in suppressing NH_3 emissions due to buffering capacity and absorptive capacity (Misselbrook and Powell, 2005).

1.4. Methane

Microbial production underlies many anthropogenic CH_4 emissions, including landfills, rice cultivation, and ruminants. Estimated ruminant (cattle, sheep, goats, etc.) CH_4 production is 87–94 Tg yr^{-1}, comparable to some estimates of natural gas pipeline losses, at 85–105 Tg yr^{-1} (IPCC, 2013). Livestock are a significant GHG source including CO_2 and CH_4 both directly from enteric fermentation and manure and indirectly from feed production (Hristov et al., 2013). CH_4 production is primarily from anaerobic fermentation of ingested plant biomass in the rumen, with long

retention time in ruminant's multiple stomachs allowing greater fermentation of recalcitrant plant materials while clearing already digested foods (Clauss et al., 2010). Fermentation is accomplished by a diverse microbial community of 360–1000 species of protozoa, fungi, bacteria, and archaea that co-evolved with the ruminants (Kong et al., 2013; Saint-Pierre and Wright, 2012). Thus, feed quality and quantity are important factors in emissions, including digestibility, which is a function of factors such as the ratio of insoluble cell wall fiber to soluble carbohydrates (Ellis et al., 2009), as well as the content of protein and other nutrients (Ellis et al., 2010). Higher fiber reduces rumen passage rates and increases CH_4 production. Climate plays a role. Whereas a temperate climate beef cow might emit 240 g d^{-1}, a tropical beef cow could emit 350 g d^{-1}, which in part relates to differences in feed for different climates (Cottle et al., 2011). This suggests that enteric emissions might have a strong seasonality and a positive feedback to climate change. Diurnal cycles of CH_4 emissions are strongly correlated with temperature (Garnsworthy et al., 2012) but also activity level, which correlates to temperature (Ngwabie et al., 2011) as well as weeks into lactation (Garnsworthy et al., 2012). Variability extends to differences between species, ages, health, etc. (Broucek, 2015), and individuals. In chamber studies, emissions from cows of the same species fed the same food were found to differ a notable ~20% (Grainger et al., 2007).

Ruminant waste produces CH_4 from bacterial processes both when freshly deposited and in storage lagoons, piles, and digesters (Montes et al., 2013), as well as from fields where applied. The primary factor is the amount of degradable organic material in the waste, which depends on feed and rumen fermentation; however CH_4 emissions also depend on the quantity of waste, the physical form of its deposit, its treatment, as well as soil conditions, aeration, weather (temperature, winds, rain), and storage treatments and duration (Broucek, 2015). Additionally, emissions exhibit time scales as microbially-produced CH_4 must migrate to the manure or slurry surface and then diffuse into the atmosphere, as must the NH_3 (Hristov et al., 2011). Clearly husbandry CH_4 emissions are complex and depend on both the real world environment and real world practices.

2. Approach

2.1. Southern California/Los Angeles basin context

In southern California, enhanced CH_4 is found in the Los Angeles Basin and much more strongly in the San Joaquin Valley, whereas coastal air generally exhibits comparatively low CH_4 concentrations (see gridded AMOG Surveyor CH_4 data, Fig. 1A). Analysis methodology is described in Leifer et al. (2016b). This map qualitatively relates to CH_4 emissions. CH_4 values in the high Sierra Nevada Mountain Range and the Mojave Desert (except downwind of Los Angeles Basin outflows) are low.

Important strong Los Angeles Basin CH_4 sources include geologic and hydrocarbon production sources (Wennberg et al., 2012) which are primarily in the basin's west and northwest, landfills that span a line from the northwest to mid-south, and husbandry from the Chino valley in the east basin (Fig. 1, immediately south of the white arrow tip). Los Angeles Basin daytime winds (Fig. 2) have a southerly component. Thus, CH_4 from geologic sources in west Los Angeles typically are transported along the foothills of the Basin's northern mountains, passing to the north of the Chino Dairy Complex.

In the Los Angeles Basin, the semi-permanent eastern Pacific high-pressure system plays a dominant controlling role in weather. This high-pressure system drives light winds and strong temperature inversions that act as a lid, restricting convective mixing to
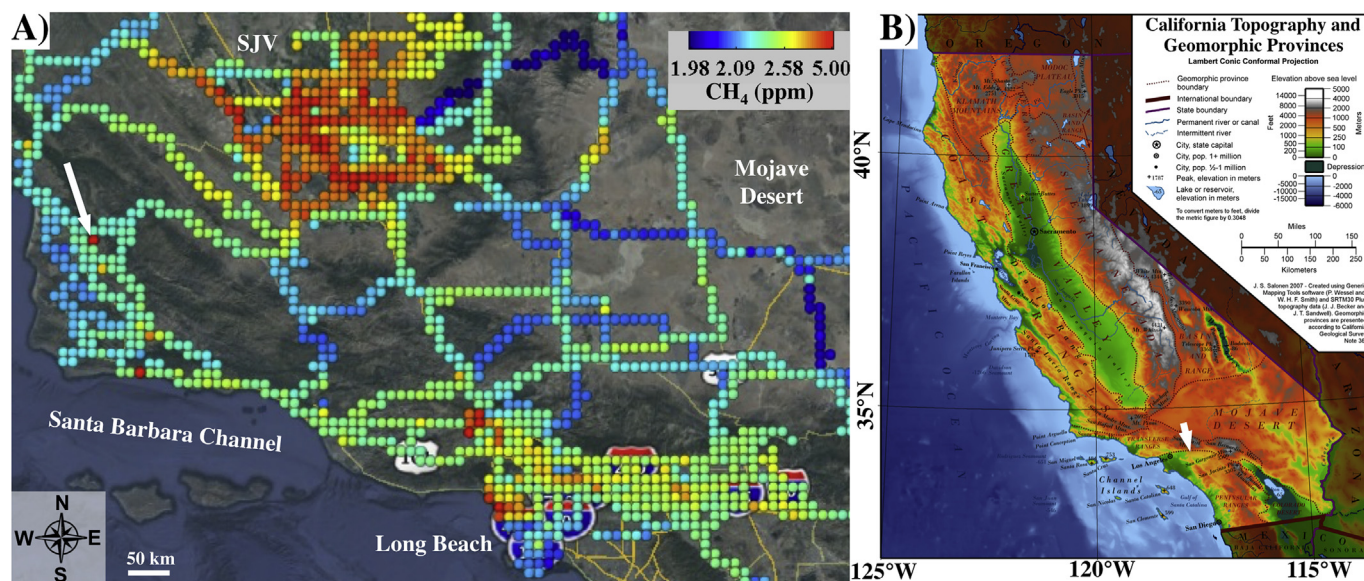
Fig. 1. A) 9-km gridded, mean methane (CH_4) concentrations from all AMOG Surveyor observations in southern California (40,340 km), Nov. 2013–Dec. 2016. Arrow shows location of the Chino Dairy Complex. Data key on figure. Colors for CH_4 concentration. **B)** California regional map including topography (Wikipedia, 2007). Arrow shows location of Chino. Legend on figure. (For interpretation of the references to color in this figure legend, the reader is referred to the Web version of this article.)

lower altitudes. Additionally, as with many other megacities, complex orography affects air quality and atmospheric transport (Gurjar et al., 2008) in the Los Angeles Basin. Specifically, surrounding mountains are physical barriers to inland transport (Lu et al., 1997), albeit imperfect. To the north lie the east-west oriented Santa Monica Mountains (600–950 m) backed by the far taller, east-west (2000–3000 m peaks) San Gabriel Mountains and the NW-SE oriented Santa Ana Mountains (1000–1700 m peaks). The Los Angeles Basin is defined to the east by the NW-SE oriented San Jacinto (3300 m peaks) and Santa Rosa Mountains (2650-m peaks). These features strongly force non-synoptic winds within an overall west-northwesterly flow (Fig. 2B).

Typical Chino area daytime winds (Fig. 2B) are from the west southwest (all year: 240–270°, June: 250–270°, see Supp. Fig. S1 for greater detail for Chino area winds) and transport emissions nearly eastwards, traversing the north-south I-15 highway (Fig. 2A). Further east, forcing by the Jurupa Hills, which rise 200–400 m above the surrounding plains and the Box Springs Mountains, northeast of Riverside, drives winds to veer to the southeast (Leifer et al., 2016b). Leifer et al. (2016b) found that just a small fraction of Chino emissions pass through the I-10 San Gorgonio Pass into the Mojave Desert. Satellite data analysis suggests most of Chino emissions pass towards the Imperial Valley/Salton Sea area (Leifer et al. (2016b).

The Planetary Boundary Layer (PBL) is shallow in the Los Angeles coastal plain and valleys and grows due to convergence and divergence of winds and downward mixing of air into the PBL (Edinger, 1959). The prevailing daytime flow is from the west (Oxnard Plain) and then through the Los Angeles Basin towards San Bernardino, rising gradually from sea level to ~400 m (Fig. 2). The transition from nocturnal to daytime winds occurs mid-morning, generally initiating at the coast and slowly shifting eastwards. For Chino, the transition generally occurs around 1100 Local Time (LT), although it varies seasonally.

2.2. Study design

2.2.1. Experimental approach

There is a growing interest in using mobile *in situ* data (airborne

or surface) to derive emissions from point sources, for pipeline leak detection/assessment and other applications (Conley et al., 2017; Leifer et al., 2016b). Data were collected by two mobile surface platforms in convoy fashion for the Chino Dairy Complex in the eastern Los Angeles Basin, Southern California on 25 June 2015 (Fig. 1). The Chino Dairy Complex herd size in 2015 was ~45,000 head (Supplemental Fig. S2). Data collection was restricted to public roads and included both *in situ* and column measurements. Data context was provided by fusion with non-concurrent airborne remote sensing data and long-term satellite trace gas observations. The platforms are described briefly below with additional details in Supplemental Section S3.

The field campaign was in June, when temperatures are warmer than the annual average. To address the literature-noted seasonality of husbandry emissions, we provide trace gas temporal context from long-term (9-years) satellite NH_3 and CH_4 data for the Chino Dairy Complex.

2.2.2. AMOG surveyor – mobile in situ concentration

Surface *in situ* data were collected by the AMOG (AutoMObile trace Gas) Surveyor, which was developed for mobile high-speed observations of trace gases, winds, and temperature. In brief, AMOG Surveyor uses a high flow vacuum pump ($850 \, L \, min^{-1}$) to draw samples down two ½" Teflon® sample lines from 5 to 3 m above ground into a bank of CEAS (Cavity Enhanced Absorption Spectrometry) analyzers as well as other analyzers for a total of 13 gases including ozone and hydrogen sulfide. *In situ* data analysis leverages multiple gas measurements – for example, Leifer et al. (2016b) used emissions of CO_2, CH_4, and NH_3 to estimate robustly herd size for a single dairy, improving emissions estimation. Additional details are provided in Leifer et al. (2018); (Leifer et al., 2014); Leifer et al. (2016b).

2.2.3. MISTIR - mobile surface column observations

MISTIR (Mobile Infrared Sensor for Tactical Incident Response) is a mobile, zenith-viewing FTIR spectrometer installed in a van that collects spectra in the 7.5–13.5 μm molecular "fingerprint" region. Calibrated spectral radiance data from the FTIR spectrometer are processed to determine column densities of gaseous constituents in
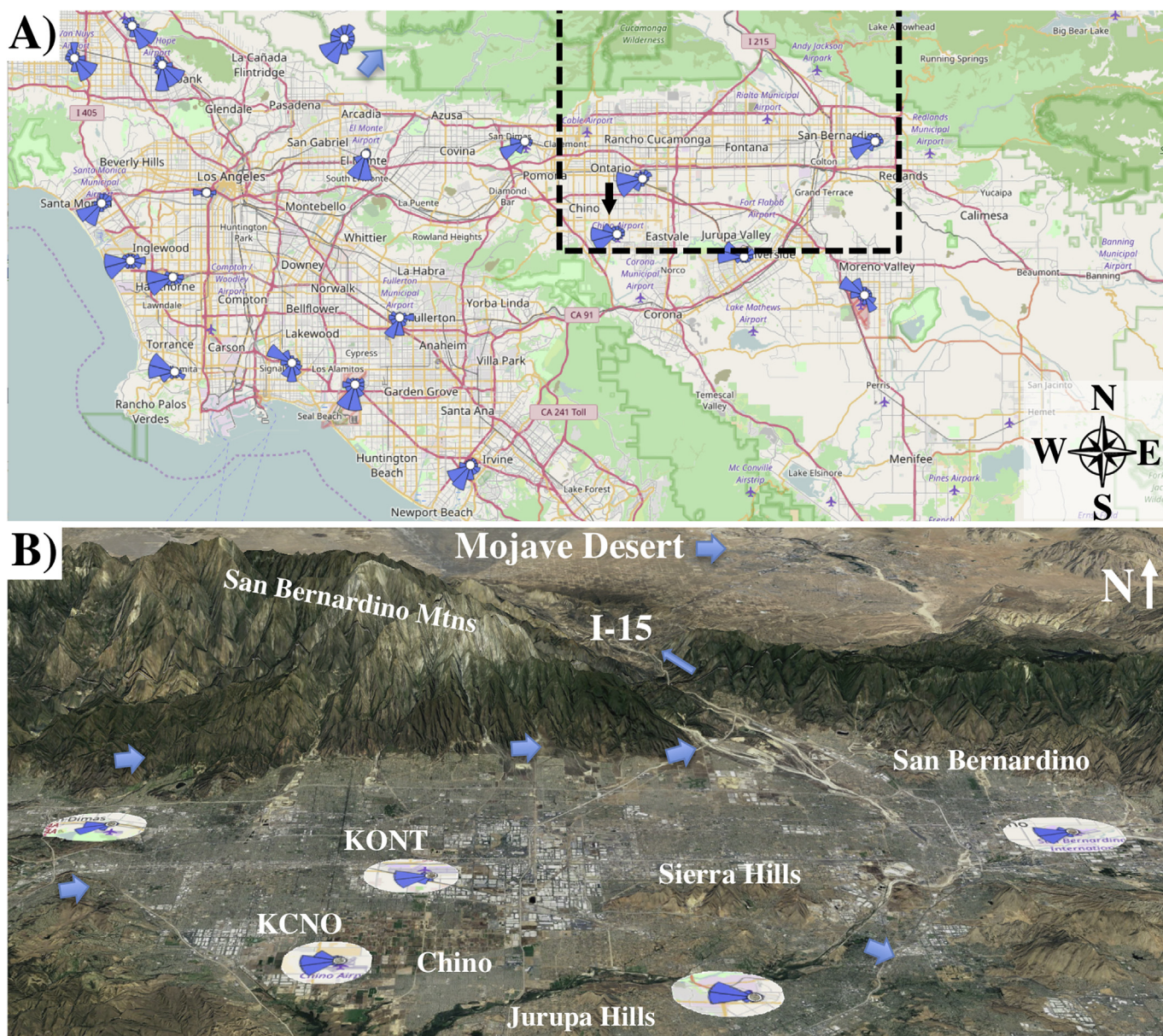
Fig. 2. A) Los Angeles Basin and surrounding area. Wind roses of wind direction probability for airport wind data (www.windhistory.com). Dashed square shows area in lower panel. **B)** Topography and typical mid-day wind patterns for the Chino Dairy Complex area for summer (Jun.–Aug.). Arrow shows Chino Dairy Complex location. Maps and imagery from Google Earth and Google Maps.

the field-of-view as well as a statistical measure (t-statistic) of the confidence in those column densities, and the fit residual.

2.2.4. Mako - airborne imaging spectroscopy observations

Imaging spectroscopy data were collected using the airborne TIR imaging spectrometer, Mako (Buckland et al., 2017), which operates in the 7.6–13.2 μm range and was flown on a Twin Otter. The procedures for detection, discrimination, and quantification of trace gas plumes are described (Buckland et al., 2017; Hall et al., 2016; Tratt et al., 2011; Young, 2002) and have separated the constituent signatures successfully of mixed plumes containing up to six distinct gaseous components in controlled trials.

NH_3 plumes depicted throughout this paper are rendered as false-color (magenta) detection images overlain on the gray-scale thermal radiance scene image. In each case, the depth of hue provides a qualitative indication of signal strength, which is a convolution of NH_3 abundance and environmental factors (i.e., the plume-surface thermal contrast).

2.2.5. IASI — space-based ammonia observations

Satellite retrievals can provide long-term trace gas temporal context for campaign data, which necessarily are limited in time and often constrained to a single season. This study uses IASI, a FTIR spectrometer. The first IASI was launched aboard MetOp-A in October 2006 with a second operating onboard MetOp-B since September 2012 (Van Damme et al., 2014). IASI flies in a polar sun-synchronous orbit with nadir overpasses at 09:30 and 21:30 local solar time at the equator and twice daily global coverage. IASI observes from 3.62 to 15.5 μm (645–2760 cm^{-1}) at a spectral resolution of 0.5 cm^{-1} and a 12-km nadir footprint (Clerbaux et al., 2009). NH_3 retrieval from IASI used the new baseline version, Artificial Neural Network for IASI (ANNI)–NH_3-v2.1 (Van Damme

et al., 2017). The new retrieval algorithm performs better throughout, especially for scenes with large thermal contrast — common in summer in east Los Angeles, and is now referenced to 0.5 km. The IASI-NH$_3$ column-retrieval uses separate neural networks for marine and terrestrial scenes.

2.3. Detailed approach

Mobile *in situ* surface trace gas and meteorology data were collected by AMOG Surveyor in convoy fashion with MISTIR with AMOG Surveyor leading due to its higher sensitivity. AMOG Surveyor and MISTIR were separated by between 5 and 20 s, providing contemporaneous *in situ* gas and meteorology data with remote-sensing column measurements.

Real-time AMOG data visualization (Leifer et al., 2014) allowed implementation of an adaptive survey strategy (Thompson et al., 2015). Surveys mapped downwind plumes and characterized the background concentrations across the region surveyed by airborne remote sensing. Specifically, real-time data were used to adjust the convoy speed to allow MISTIR to collect higher spatial resolution data within plumes than outside. Real-time data helps to improve plume characterization by informing repeat survey data collection. This is very important given that some plumes were transient with respect to the measurement transects. Real-time data from Google Maps™ (Wu et al., 2007) aids survey navigation to avoid traffic, a significant consideration in the Los Angeles Basin, allowing alternative route selection to avoid traffic blockages. Additionally, real-time weather from pre-selected weather stations was monitored to provide a regional understanding of evolving meteorological conditions during the survey.

MISTIR column data can observe plumes anywhere in the atmospheric column, including plumes that have not diffused to the surface (where AMOG Surveyor measures). This arises in the case of strongly buoyant plumes, e.g., large pipeline (production or transport) leaks (Conley et al., 2016; Leifer et al., 2016a). For husbandry and agricultural emissions; however, sources are dispersed and generally from non-buoyant to weakly buoyant. The validity of the assumption that buoyant rise was not significant was tested by comparing modeled AMOG Surveyor and MISTIR data, which also validates plume turbulence assumptions in the inversion plume model (Section 2.4) used to derive emissions (Leifer et al., 2016a). MISTIR is highly sensitive to NH$_3$, but only weakly sensitive to CH$_4$. The validated AMOG atmospheric characterization then was applied to derive CH$_4$ emissions from AMOG data.

Supporting airborne remote sensing data were collected by Mako on a Twin Otter on 25 July 2014 with concurrent AMOG Surveyor data; see Leifer et al. (2016b) for details. In Leifer et al. (2016b), a single transect of data was analyzed to calculate emissions from the Chino Dairy Complex, whose representativeness depends on the extremely large number of emission sources.

2.4. In situ and column plume inversion

Plume inversion to derive emissions and source locations from *in situ* data used a Gaussian plume model based on observed winds and error minimization with the measured concentration anomaly (C') profile during lateral transects across the plume. Emissions derivation from column data combines winds with transect profile column data plume anomaly.

Absolute winds are calculated from AMOG relative winds after filtering and accounting for vehicle motion. Specifically, the north and east wind components are filtered with a 2-s, running median-filter. Poor transient wind readings arise from other large vehicles (trucks and buses) and structural obstacles in conjunction with cross winds near the downwind side of the road and structures

near the downwind side of the road. Cars tend not to affect wind observations due to the height of the anemometer and because cars are fairly streamlined, unlike larger vehicles. AMOG velocity, acceleration, and rate of turn are used to quality-flag wind data. If the rate of turn is greater than $5° \, s^{-1}$ or the acceleration is greater than $1 \, m \, s^{-2}$, winds are flagged as unreliable and replaced by linear interpolation. Absolute wind velocities are calculated by subtracting filtered GPS vehicular motion. Then, absolute winds are smoothed with a median filter of varying length from 0 to 50 s depending on the wind data variability. The plume inversion uses the spatial-average of winds spanning the plume. Thus, finer-scale turbulence structures are not preserved for the calculations, although close inspection of finer-scale wind structure is made to identify potential orographic forcing.

The plume model inversion is a three-step process. First, transect data, which are collected approximately perpendicular to the winds, are projected in the wind direction onto the transect line to correct for road deviations from a straight line orthogonal to the wind. Then, C' data are fit by a linear combination of one to several Gaussian functions, termed the data model. See Supplemental Section S.4 for an example two-plume data model for the Chino Dairy Plume. The data model is derived by error minimization using a least-squares linear-regression analysis (Curve Fitting Toolbox, MatLab, Mathworks, MA). The number of sources was determined by inspection of the *in situ* plume transect profile shape, by investigation of the error reduction from modeling additional sources, and by consideration of reasonable source distances.

Next, a Gaussian plume model (Hanna et al., 1982) is optimized for each data model Gaussian function by error minimization to optimize for the source location and strength, after Leifer et al. (2016b). Source locations are not forced to lie within a dairy, although CH$_4$ plumes that are missing NH$_3$ are presumed to originate from a non-husbandry source, such as a pipeline leak, and thus are not aggregated into the husbandry emissions. This inversion is termed an uninformed model as it relies solely on *in situ* data from a single gas without recourse to ancillary remote sensing and other *in situ* trace gas data. The Gaussian plume model uses the mean wind speed (u) over the plume's dimensions and assumes constant winds over the time of flight from the source to the data transect. The plume model estimates the source emissions (E_{AMOG}) based on the measured C' for the along-wind, transverse, and vertical dimensions (x, y, z, respectively) given by:

$$C'(x,y,z) = E_{AMOG} \frac{\exp\left(\frac{-y^2}{2\sigma_y^2}\right)}{(2\pi u \sigma_z \sigma_y)} \left(\exp\left(\frac{-(z-h)^2}{2\sigma_z^2}\right) + A \exp\left(\frac{-(z+h)^2}{2\sigma_z^2}\right) \right) \tag{1}$$

where h is plume origin height, set to 0 m for weak, non-point source agricultural plumes, σ_y and σ_z are atmospheric turbulence parameters, and A is a stickiness parameter. The second exponential term represents reflection off the earth's surface for non-sticky molecule, e.g., A (NH$_3$) = 0; A (CH$_4$) = 1. C' is relative to the background concentration, C, which is based on a linear fit to C outside the plume boundaries allowing for environmental gradients from large-scale transport.

The Gaussian plume model has a number of underlying assumptions. Specifically, it is for a passive (non-reactive, non-sticky) dispersant, negligible along-wind diffusion, winds along the x-axis, a vertically uniform u, and winds where the fluctuation component of u is zero. These assumptions imply an idealized flat terrain, discussed below. Turbulence parameters are available for a range of different stability classes Briggs (1973), provided in Supplemental

Section S.5. For this analysis, we improve on the discrete Briggs (1973) turbulence parameterization by a linear model with respect to u.

Due to its column measurement, estimating emissions by MISTIR (E_{MISTIR}) is straightforward, involving the product of the integrated column concentration anomaly (XC') with the vertical wind profile ($u\,(x, z)$) across the transect plane:

$$E_{MISTIR} = \int_{x1}^{x2} XC'(x) \int_{0}^{z=PBL} u(x,z)\ dzdx \qquad (2)$$

where $u(z)$ is assumed uniform and is provided by AMOG Surveyor. Thus, E_{MISTIR} provides validation of the appropriateness of the Gaussian plume model (1) assumptions, while airborne Mako data provides validation of source location.

3. Results

3.1. Greater Los Angeles basin regional context

IASI full-atmosphere NH_3 retrievals averaged for 2008–2016 (Fig. 3A) shows the Chino Dairy Complex is by far the dominant Los Angeles Basin NH_3 source. A smaller, secondary source is from the Riverside Dairies, ~55 km to the east-southeast of the Chino dairies. Much lesser emissions originate from north of the Los Angeles Airport (LAX) and the Port of Los Angeles, likely industrial; however, downtown Los Angeles, where traffic is heaviest, is not a

significant source, as observed by Leifer et al. (2016b). There was excellent spatial agreement between the AMOG surface NH_3 observations on 25 June 2015 and IASI for the Chino area, showing the importance of prevailing winds to defining the near field fate of the dairy NH_3 emissions. The overall NH_3 plume trends east and then southeast, a flow pattern noted in Leifer et al. (2016b).

The agricultural regions of the San Joaquin Valley are a far stronger NH_3 source than the Los Angeles Basin, with both AMOG and IASI showing a decrease in NH_3 for the western flank of the south San Joaquin Valley where agriculture gives way to fossil fuel production (Fig. 3B, black arrow). Air mass movements cause AMOG-IASI disagreement in the Bakersfield area and north, with significant change evident between AMOG's ascent and descent of the Sierra Nevadas – separated by just a few hours. At elevation in the Sierra Nevada, both AMOG and IASI decrease towards background. Both AMOG and IASI observe low NH_3 and CH_4 in the Mojave Desert.

IASI 0–4 km column methane (XCH_4) for 2010–2016 (Fig. 3B) was gridded with 0.75° windows, with 53% overlap (0.04°) to bring out fine spatial-scale structures. XCH_4 retrievals for 2008–2009 were not used as the algorithms were revised for stability in 2010 (X. Xiong, NOAA, Pers. Comm., 2015). The XCH_4 map shows high concentrations from numerous strong basin CH_4 sources, mostly from the western Los Angeles Basin where oil production and geologic migration from petroleum reservoirs (Peischl et al., 2013) which provides important CH_4 sources, as do emissions from the natural gas distribution network. The CH_4 plume from the Chino Dairy Complex is outlined in dotted white in Fig. 3B, inset, and follows two trends. The first is due east, and the second is east and
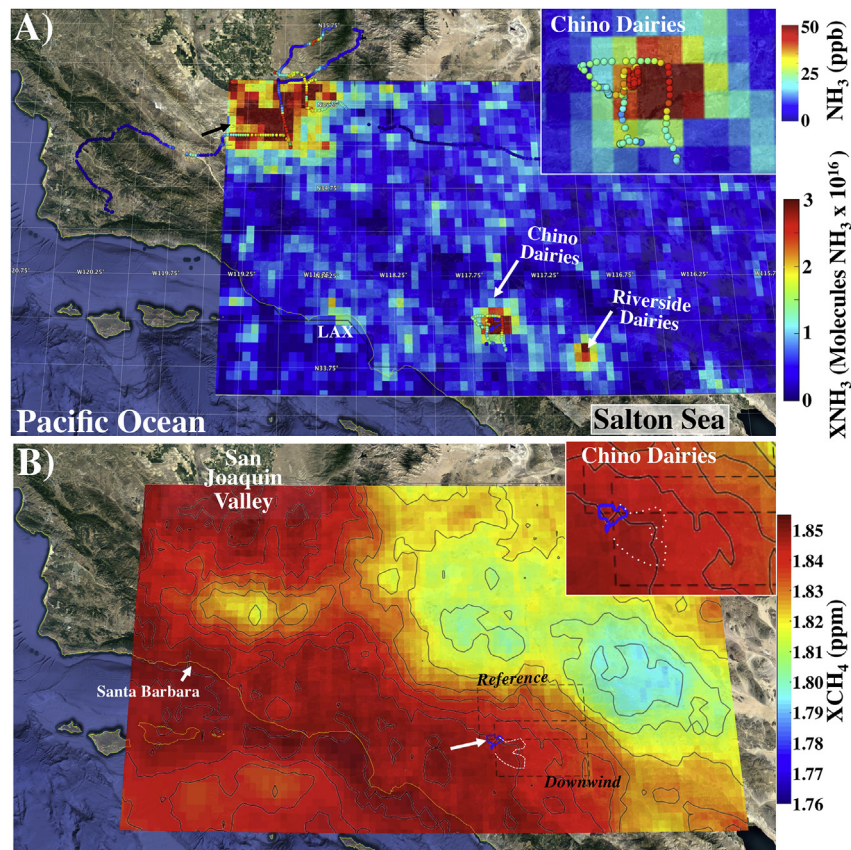
Fig. 3. **A).** IASI full atmosphere column ammonia (XNH_3) map of Los Angeles Basin Area, 2008–2016, and all AMOG *in situ* ammonia (NH_3) data collected 25 June 2015. Inset shows zoomed in area of Chino Dairy Complex (blue outline). **B)** IASI mean 0–4 km methane column concentration (XCH_4) map (2010–2016), locations of Chino Dairy Complex (blue outline) and Chino reference and downwind boxes for trend analysis, labeled. Chino Dairy Complex CH_4 plume outlined in dotted white line, see inset. Contours every 10 ppb 1790–1830 ppb, 5 ppb–1860 ppb. Data keys on figure. Shown in the Google Earth environment. (For interpretation of the references to color in this figure legend, the reader is referred to the Web version of this article.)

then southeast. This pattern is dictated by orography, specifically the Jurupa Hills to the east (Leifer et al., 2016b). The CH$_4$ plume is approximately 5 ppb above local ambient. Strongly elevated XCH$_4$ also is observed in the San Joaquin Valley.

3.2. Chino Dairy Complex

In the 1920s, urbanization pressures induced approximately 100 dairies in the San Fernando Valley to move to the east Los Angeles basin, settling in San Bernardino County while still serving the Los Angeles dairy market (Leifer et al., 2016c). Herd size was 145,000 cows in 1972, reaching 163,304 cows in 1999 — the densest in the U.S (Peterson, 2000). However, urbanization pressures combined with inexpensive refrigerated shipping from the San Joaquin Valley to Los Angeles began taking a toll on Chino Dairy production (Leifer et al., 2016c). In 2002, herd size was 152,000 cows on 184 dairies, which produced 1.5 billion kg yr^{-1} milk, decreasing to 45,196 cows on 63 dairies in 2015 that produced 540 million kg milk annually (Supplemental Fig. S2). Herd size 2009–2012 was 75,000 cows, decreasing to 45,000 cows 2015–2016 with concomitant decreases in milk production, albeit at higher per cow efficiency (CDFA, 2002–2017). Trends in Chino have been the opposite of trends for California with state milk production increasing ~20% from 2002 to 2005 and remaining steady since — i.e., the Chino herd shifted elsewhere in California (Cottle et al., 2011). Additionally, there are several small poultry operations in the Chino Dairy Complex (CDFA, personal communication, 2018).

Cows are primarily Holsteins, with year-round milk production

on a 12–13 month cycle and a two month dry period (CDFA, personal communication, 2018); yet, despite management efforts, some seasonality remains in milk production with a maximum in April (Supplemental Fig. S3), corresponding to the calving season. The primary dairy rations are alfalfa hay, which is fed free-choice on manger floors two or three times per day (Peterson, 2000). Added to this are grain and bi-product ingredients including rolled barley, cottonseed, dried beet pulp, hominy, and wet citrus pulp. Animals then are grouped and fed according to production. For example, grain is fed in milking barns to allow high producing cows to consume extra feed.

There is some seasonality in feed for Kern County dairies in the San Joaquin Valley due to the availability of silage and alfalfa; however, silage is far less accessible to San Bernardino dairies and thus feed is more constant. Calves are birthed at the facilities and sent to calf nurseries elsewhere, although a few of the older Chino Dairies rent corrals to raisers. Overall, herd age is fairly constant and does not vary seasonally, with heifers generally on a 2-year replacement schedule (CDFA, personal communication, 2018).

Chino dairies are older and smaller than most dairies in the San Joaquin Valley, and do not have fans to cool the cow sheds; however, temperatures in the Los Angeles Basin are more moderate than in the San Joaquin Valley. Underlying this could be the smaller typical dairy size, which is ~800 cows. The small size of these dairies reduces economies of scale. As a result, 24/7 illumination for operations that is becoming common in the San Joaquin Valley are absent in Chino (CDFA, personal communication, 2018).

Chino waste management is dry (Google Earth suggests at most
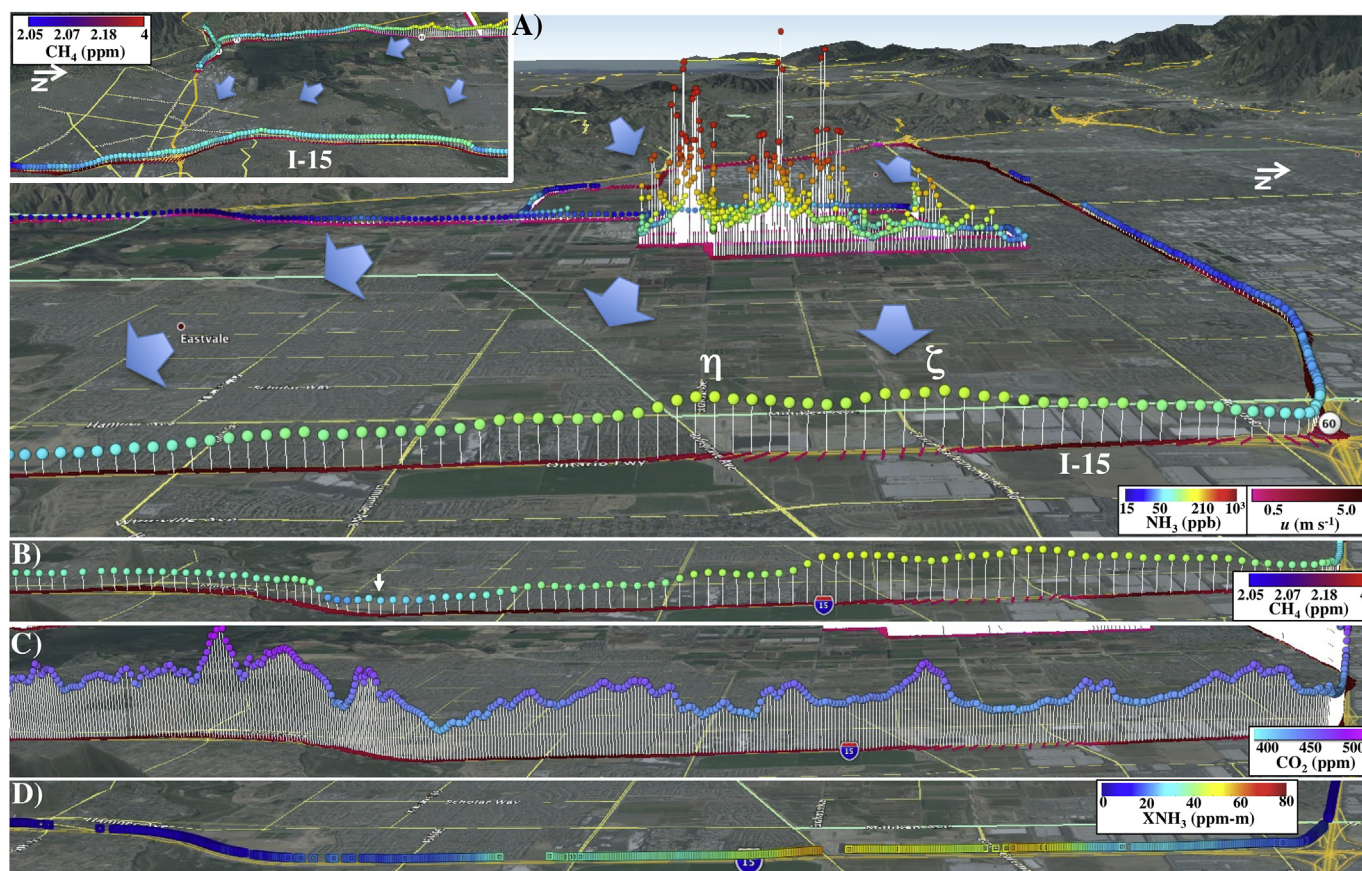
Fig. 4. A) *In situ* ammonia (NH$_3$) and wind speed (u) downwind of the Chino Dairy Complex for 25 June 2015. Arrows show overall wind patterns. Peaks of plumes used in the Gaussian inversion model labeled (ζ, η). **Inset.** Methane (CH$_4$) to the south of Chino and arrows illustrating downfield airflow. North edge of inset data matches white arrow in panel B. **B)** *In situ* CH$_4$, same view as in panel A. **C)** *In situ* carbon dioxide (CO$_2$) on the I-15 transect, same view as in panel A. **D)** MISTIR column NH$_3$ (XNH$_3$) on the I-15 transect, same view as in panel A. Shown in the Google Earth environment.

one lagoon) with waste typically spread on open areas near the dairy, not piled, with the exception of one dairy near the Chino airport (Leifer, personal observations, 2015). Cow feeding aprons are covered with waste that is moved daily to nearby fields to dry. Waste is scraped several times a year from these fields prior to the rainy season, mid-fall, and afterwards in mid-spring (CDFA, personal communication, 2018).

3.2.1. Outflow plume

On 25 June 2015, daytime wind patterns were from 260°, typical for summer (for Chino summer prevailing winds see Supp. Fig. S1). Air with enhanced CH_4 and NH_3 flowed into the Chino Dairy Complex from the heavily populated Los Angeles County to the west and from Orange County through a canyon that crosses Chino Hills (Fig. 4A). As winds traversed the Chino Dairy Complex they manifested a large-scale divergence as a northerly component to the north, and a southerly component to the south, loosely corresponding to the northwest-southeast orientation of the Chino Hills. By continuity, this divergence corresponds to down-mixing and downwelling of relatively cleaner, higher altitude air crossing the Chino Hills.

The Chino Dairy Complex plume was observed during a downwind north to south transect on I-15 (Fig. 4) with in situ NH_3 reaching 82 ppb and a clearly collocated CH_4 plume reaching 2167 ppb (~110 ppb above ambient). CO_2 showed elevated levels but no clear plume (Fig. 4D), likely confounded by traffic emissions. The CH_4 and NH_3 plumes were broad and comparable to the Chino Dairy Complex's width (5–8 km). This transect was collected at

1.8 km min^{-1}, i.e., plume transit was just a few minutes.

Although surface winds were measured from the rightmost (upwind) lane, as in 2014, see Leifer et al. (2016b), winds on I-15 were more complicated in these data. By inspection and comparison with the overall Chino Dairy wind flow (not highway data), it was determined that wind measurements only were accurate for the segment between the two NH_3 peaks (Fig. 4A η - ζ) where there was an absence of large, upwind warehouse structures. Wind speeds were 2.8 m s^{-1} for this segment. Outside this segment, winds were strongly aligned with traffic (northerly). The high CO_2 concentrations observed are consistent with this interpretation (Fig. 4D). One explanation is that the large upwind buildings weaken the cross winds so that they no longer advect traffic-associated airflow out of the upwind lane where data were collected. This interpretation is supported by wind data collected on small roads across the Chino Dairy Complex (3.2 m s^{-1}) being largely westerly. Despite being in the heavily urbanized Los Angeles Basin, the Chino Dairy Complex is rural in character — open fields with few structures and virtually no traffic. Winds were measured during surveys in the Chino Dairy Complex ~1 h before the I-15 transit, i.e., approximately Lagrangian. Additional support for this wind interpretation is provided by comparison with prior data (Leifer et al., 2016b) where winds consistent with the plume structure (westerly) were measured for the entire I-15 transect under significantly stronger cross-winds.

The plume inversion assumes constant u with altitude. A comparison of the column NH_3 (XNH_3) and in situ NH_3 and CH_4 data showed similar overall plume widths and dual peak shape, albeit
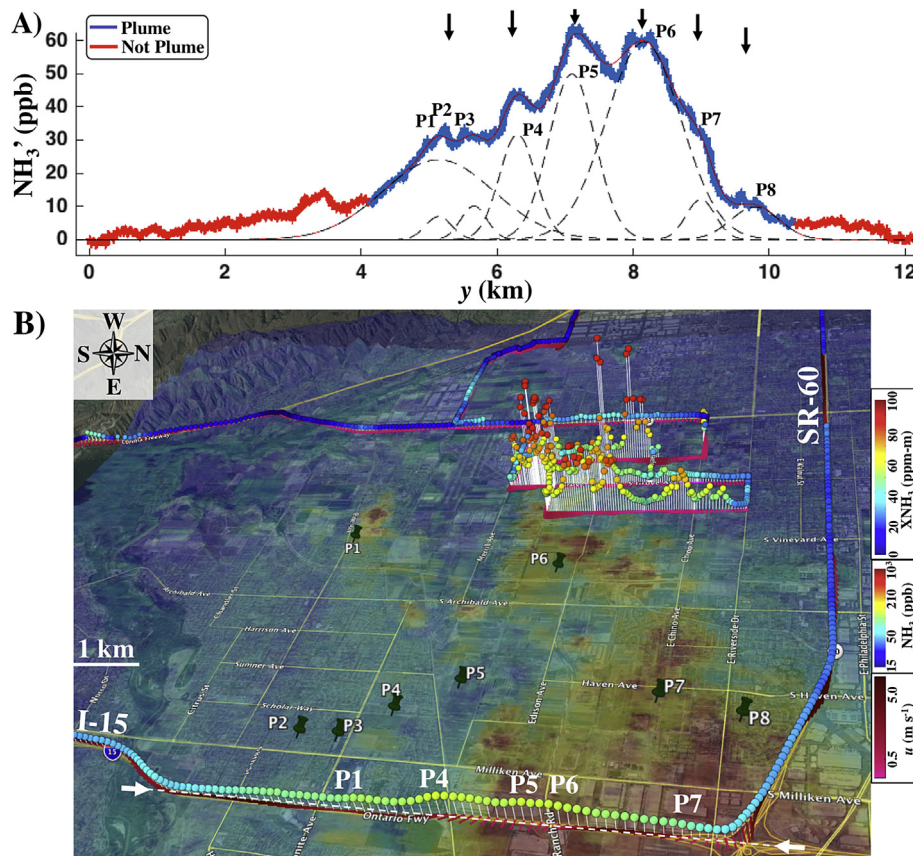
Fig. 5. Eight-plume informed (8I) model for I-15 downwind (north to south) transect with respect to arbitrary lateral distance (y) for **A)** ammonia anomaly (NH_3') and winds (u) versus (y). Plume peaks labeled. Arrows show transect features modeled that suggested a six-plume uninformed model (not shown). **B)** In situ NH_3 and u superimposed on Mako XNH_3 data for 25 Jul. 2014, 1820–1846 UTC (1020–1046 LT), and the 8I model-projected plumes' origins. Selected transect plume features labeled. White arrows bracket the transect line onto which transect data are projected. Data key on figure. Shown in the Google Earth environment.

with a ~220 m offset. The offset was based on comparing single Gaussian function fits to the column and *in situ* data for plumes from sources many kilometers distant. This small offset represents up to a few degrees of wind veering (over the vertical height of the plume), indicating wind veering with altitude is small. This is unsurprising given the strong orographic forcing for this plume which is mostly to completely shallower than the surrounding orographic features.

In situ derived emissions (E_{AMOG}) were for both uninformed (based solely on single gas transect data) and informed (by additional data including other trace gases and airborne and surface remote sensing) plume inversion models for comparison with E_{MISTIR}. Guidance also was provided by Mako airborne NH_3 retrievals from 25 July 2014 (Fig. 5B), i.e., the same season. Google Earth imagery and upwind *in situ* data provided guidance for informed inversion models of dairies with evident emissions in the remote sensing data. Note, Google Earth imagery can be out of date, for instance some dairies in Google Earth imagery now are residential sub-divisions.

A key inversion step is identifying the transect plume structures to model, which aids in defining the background. The northern plume edge was at y~10.3 km, beyond plume P8 (Fig. 5). The plume's south edge was based on a wind-direction projection onto

the I-15 transect of the southern-most Chino Dairy (Fig. 5B, just west of plume P1 source). This corresponded fairly closely with the sharper edge observed in XNH_3' data (Fig. 6D).

South of the plume's edge ($y < 4.3$ km), the north to south NH_3' trend showed a slow decrease from ~10 ppb at y~4 km to 0 ppb at y~0 km, the same as at the north plume edge. This decrease appears to be from instrumentation latency with a timescale of ~1 min; however, Mako data (Fig. 5B) show that the extensive suburban developments to the south of Chino correspond to a broad area NH_3 source with additional sources from agricultural fields further to the west (see Fig. 9). Thus, the decreasing *in situ* NH_3 trend likely is real, not instrumental. This area also corresponded to elevated CH_4 (Fig. 4B), suggesting legacy soil emissions from former dairies, now subdivisions.

Mako data show that Los Angeles Basin background XNH_3, e.g., west and upwind of Chino, was significantly elevated in the Chino area, both in suburban developments to the north and to the south. Notably, a similar XNH_3 elevation was not observed in the suburban communities to the west. The Chino area enhancement was confirmed by AMOG *in situ* data, with Chino ambient levels of ~12 ppb. This enhancement strongly suggests remnant legacy NH_3 emissions, discussed below.

The inversion calculation (Eqn. (1)) used $u = 3$ m s^{-1} from 260°
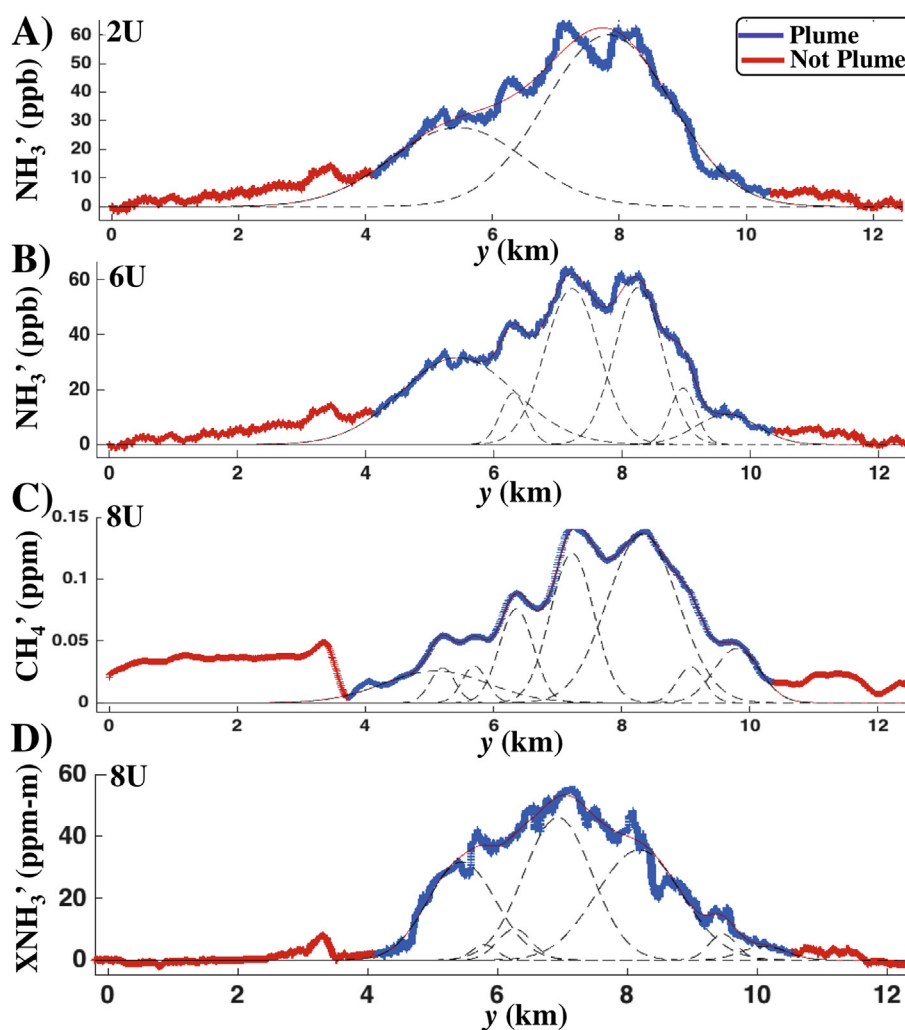
Fig. 6. Chino downwind I-15 plume transect with respect to arbitrary lateral distance (y) for **A)** AMOG ammonia anomaly (NH_3') and two plume uninformed (2U) model, **B)** AMOG NH_3' and six plume uninformed (6U) model, **C)** AMOG methane anomaly (CH_4') and eight plume informed (8I) model, **D)** MISTIR NH_3 column anomaly (XNH_3') and eight plume uninformed (8U) model. Data key on figure.

Table 1
Uninformed and informed NH_3 plume inversion model for the Chino Dairy Complex.

#	2U-AMOG E ($Gg\ yr^{-1}$)	D (km)	6U-AMOG E ($Gg\ yr^{-1}$)	D (km)	8I-AMOG E ($Gg\ yr^{-1}$)	D (km)	8I-MISTIR E ($Gg\ yr^{-1}$)	D (km)	8I-2-AMOG E ($Gg\ yr^{-1}$)	D (km)	8I-2-MISTIR E ($Gg\ yr^{-1}$)	D (km)
1	8.9	8.10	6.89	6.50	4.40	5.90	5.76	5.61	4.52	5.61	5.76	5.61
1B					0.05	1.10	0.06	1.10	0.06	1.10	0.06	1.10
1C					0.08	1.10	0.15	1.12	0.09	1.12	0.15	1.12
2	24.8	9.30	0.19	1.25	0.54	1.65	0.63	1.65	0.60	1.65	0.63	1.65
3			2.8	2.85	1.45	2.15	3.13	2.15	1.59	2.15	3.13	2.15
4			3.3	3.10	7.90	5.00	5.06	4.75	8.25	4.75	5.06	4.75
5			0.56	2.10	0.33	2.00	0.52	2.07	0.37	2.07	0.52	2.07
6			0.5	2.70	0.11	1.35	0.39	1.35	0.12	1.35	0.39	1.35
Tot	33.8		14.2		14.9		15.7		15.6		15.7	

*Model descriptor is NU or NI where N is number of plumes, U − Uninformed, I − Informed, and I-2 − Turbulence optimized. E is the NH_3 emissions and D is distance.

based on the average of wind observations across the Chino Dairy Complex and further west. As wind data were collected approximately Lagrangian, this average should represent the winds integrated over the plume's trajectory. Combining u with XNH_3 (Eqn. (2)), yields E_{MISTIR} (NH_3) = 15.7 $Gg\ yr^{-1}$.

Based on the overall shape, the *in situ* CH_4 and NH_3 plumes were modeled first as an uninformed dual Gaussian plume (2U) (Fig. 6A). See Tables 1 and 2 for inversion model results. This is an evident simplification that neglects fine-scale structure − i.e., assumes emissions are in two large dominant plumes with small-scale structures being "noise." In this interpretation, noise arises from wind heterogeneity such as divergence and convergence flows (often induced by structures and orography), and from near-field, weak sources. E_{AMOG} (NH_3)$_{2U}$ was 34 $Gg\ yr^{-1}$, over double E_{MISTIR} (NH_3). E_{AMOG} (CH_4)$_{2U}$ was a similarly large 42.5 $Gg\ yr^{-1}$. The mean trace gas emissions ratio (R_E), defined as:

$$R_E = \frac{E_{Amog}(NH_3)}{E_{Amog}(CH_4)} \quad (3)$$

was 0.80. Plume numbering is based on south to north source location. Plume P2 dominated, contributing 74% of E_{AMOG} (NH_3)$_{2U}$ and 83% of E_{AMOG} (CH_4)$_{2U}$. Plume source distances (D) were 9.3 and 8.1 km, for plumes P1 and P2, respectively, i.e., at the complex's far end. This disagreed with *in situ* concurrent observations that supported many active dairies, many of which were closer (Fig. 5) and with Mako data that showed significant emissions from numerous Chino dairies. As Mako data were from the year prior, the *in situ* data confirmed that many dairies remained active sources. The 2U model clearly was poor.

Inspection of the AMOG NH_3 transect data suggested a six plume

model (6U) would capture large-scale features that clearly were not "noise." The inversion yielded E_{AMOG} (NH_3)$_{6U}$ = 14.2 $Gg\ yr^{-1}$ (Fig. 6B), ~90% of E_{MISTIR}. The dominant contribution was from plume P1, which accounted for almost half of overall NH_3 emissions (6.9 $Gg\ yr^{-1}$) from a source at D = 6.5 km.

MISTIR data (Fig. 6D) confirmed background NH_3 concentrations were chosen appropriately. The NH_3 plume at y~3.5 km in both MISTIR and AMOG data originates in suburban neighborhoods, was discrete from the main dairy complex plume, and was not incorporated into the current analysis. As discussed below, this plume may relate to legacy emissions.

The AMOG CH_4 transect clearly showed 8 plumes and a 6U CH_4 model could not be derived, i.e., failed to converge. For reference, a 6I CH_4 model inversion was run by forcing the plume locations and widths from the 6U NH_3 model. E_{AMOG} (CH_4)$_{6I}$ was 29.5 $Gg\ yr^{-1}$ with most of emissions arising from three plumes (P3-39%, P4-26%, and P2-21%).

E_{AMOG} (CH_4)$_{8U}$ was 30.3 $Gg\ yr^{-1}$ and was dominated by plume P4 (19.0 $Gg\ yr^{-1}$). Whereas plume P1 was dominant in the 6U NH_3 model, the 8U model partitioned plume P1 into three plumes, with a new, more southerly plume P1 originating from D = 5.9 km, near a strongly emitting dairy in the Mako retrieval (Fig. 5A). The 8U CH_4 model (Fig. 6C) was used to inform the locations and widths of an 8-plume (8I) NH_3 model. This forces the same source distances. E_{AMOG} (NH_3)$_{8I}$ was 14.9 $Gg\ yr^{-1}$ − 95% agreement with E_{MISTIR}. Plume P6 also dominated NH_3 emissions (51%). NH_3 emissions for plumes P1, P2, and P3 (formerly P1 in the 6U NH_3 model at 6.9 $Gg\ yr^{-1}$) were 4.40, 0.05, and 0.08 $Gg\ yr^{-1}$, respectively, and were consistent with the relative anomaly strengths in the Mako data for nearby sources (Fig. 5B). R_E for five of eight plumes were similar, 0.38−0.46, including the dominant plume, P4, suggesting similar husbandry

Table 2
Uninformed and informed CH_4 plume inversion model for the Chino Dairy Complex.

#	2U-AMOG E ($Gg\ yr^{-1}$)	D (km)	R_E	6U-AMOG E ($Gg\ yr^{-1}$)	D (km)	8I-AMOG E ($Gg\ yr^{-1}$)	D (km)	R_E	8I-2-AMOG E ($Gg\ yr^{-1}$)	D (km)	R_E
1	17.6	7.20	0.51	39.1	6.5	4.74	5.90	0.93	4.58	5.61	0.99
1B						0.23	1.10	0.22	0.23	1.08	0.26
1C						0.24	1.10	0.33	0.24	1.08	0.38
2	82.4	8.20	0.30	1.5	1.25	1.30	1.65	0.42	1.31	1.60	0.46
3				21.5	2.85	3.50	2.15	0.41	3.56	2.12	0.45
4				26.1	3.1	18.97	5.00	0.42	19.28	4.92	0.43
5				4.2	2.1	0.79	2.00	0.42	0.80	2.00	0.46
6				7.7	2.7	0.54	1.35	0.20	0.54	1.35	0.22
Tot	100		0.34	100		30.3		0.00	30.5		
Mean			0.40					0.42			0.46
std			0.15					0.22			0.23

*Model descriptor is NU or NI where N is number of plumes, U − Uninformed, I − Informed, and I-2 − Turbulence optimized. E is CH_4 flux, D is distance, and $R_E = E_{NH3}/E_{CH4}$.

practices. Two of the smallest plumes exhibited significantly lower R_E, 0.26 and 0.22 (plumes P8 and P6, respectively), indicating processes that favor CH_4 emissions, whereas one plume, P1, strongly favored NH_3 emissions ($R_E = 1.0$).

The shape of the MISTIR XNH$_3$ transect suggested a single-plume uninformed (1U) model was inappropriate for XNH$_3$. Instead, the 8U CH$_4$ model was used to inform an 8-plume (8I) model for MISTIR to derive the relative plume strengths. Specifically, the 8U CH$_4$ model specified source location and widths, and y (plume centerline) was allowed to vary (Fig. 6D).

Agreement for the relative importance varied widely between plumes (from 46 to 156%). For plumes P1-P3, agreements were 76%, 83%, and 53%, respectively. In contrast, agreement was poor (46%) for the strongest plume (P6). MISTIR data showed several features where the trend decreased far more steeply than the model could predict, particularly for plume P1 at the south edge. This likely reflects the effect of (slight) wind veering with altitude. As with the AMOG models, the 8-plume MISTIR model brought source locations closer.

Still, there was fine-scale structure in the transect data that the 8I model failed to capture. To explore the implications of missing these structures, a twelve-plume, uninformed (12U) NH$_3$ model was developed, and yielded E_{AMOG} (NH$_3$)$_{12U}$ = 9.5 Gg yr^{-1}. The increased number of plumes, many of whose sources were closer than 1 km where there was an absence of near-field dairies, significantly worsened agreement with E_{MISTIR}.

One source of uncertainty in the model is the turbulence parameterization, which could be underestimated due to forcing by structures. Hanna et al. (1982) recommended a one stability class increase (less stable) for the urban environment. We tested the hypothesis that upwind structures decrease stability by optimizing the 8I-2 NH$_3$ model to force $E_{AMOG} = E_{MISTIR}$ and found a small increase towards Stability Class A (a increased from 0.19 to 0.20; b from 0.16 to 0.168 (Supplemental Section S5 for description), equivalent to a decrease of u to 1.9 m s^{-1}. This turbulence-optimized model slightly increased E_{AMOG} (CH$_4$)$_{8I-2}$ to 30.5 Gg yr^{-1} and affected the two strongest plumes (P4 and P1), bringing them a few hundred meters closer. Very small changes also were introduced in the other plumes. It also very slightly increased the values and spread of R_E from 0.42 ± 0.22 to 0.46 ± 0.23. In fact, with the exception of plume P1 ($R_E = 0.99$) and two very small plumes that contributed a combined 2.8% of total emissions (P6, P8), the average R_E for the other five plumes was 0.43 ± 0.04%, suggesting similar husbandry practices.

It is worth noting that these emissions, while in line with other published Chino studies are for approximately 45,000 cows, far less than suggested in other studies, and was based on California Department of Food and Agriculture statistics (CDFA, 2002–2017). As a result, these results suggest Chino husbandry emission factors could be significantly greater than suggested in previous literature.

Given the time gap between the Mako acquisition and the AMOG/MISTIR survey, no attempt was made to quantitatively analyze the Mako data. Nevertheless, a highly prominent feature in the Mako data merits note - a massive NH$_3$ cloud northeast of I-15. Integration of the retrieved NH$_3$ column yielded 8 Gg NH$_3$, an amount that cannot be explained by husbandry emissions (it is on the order of annualized Chino emissions). Moreover, a husbandry NH$_3$ cloud of this strength would have an easily detectable, associated CH$_4$ cloud, which was not observed. Thus, the most feasible explanation is an accidental NH$_3$ release, presumably industrial, which therefore likely arose from outside the Chino Dairy Complex.
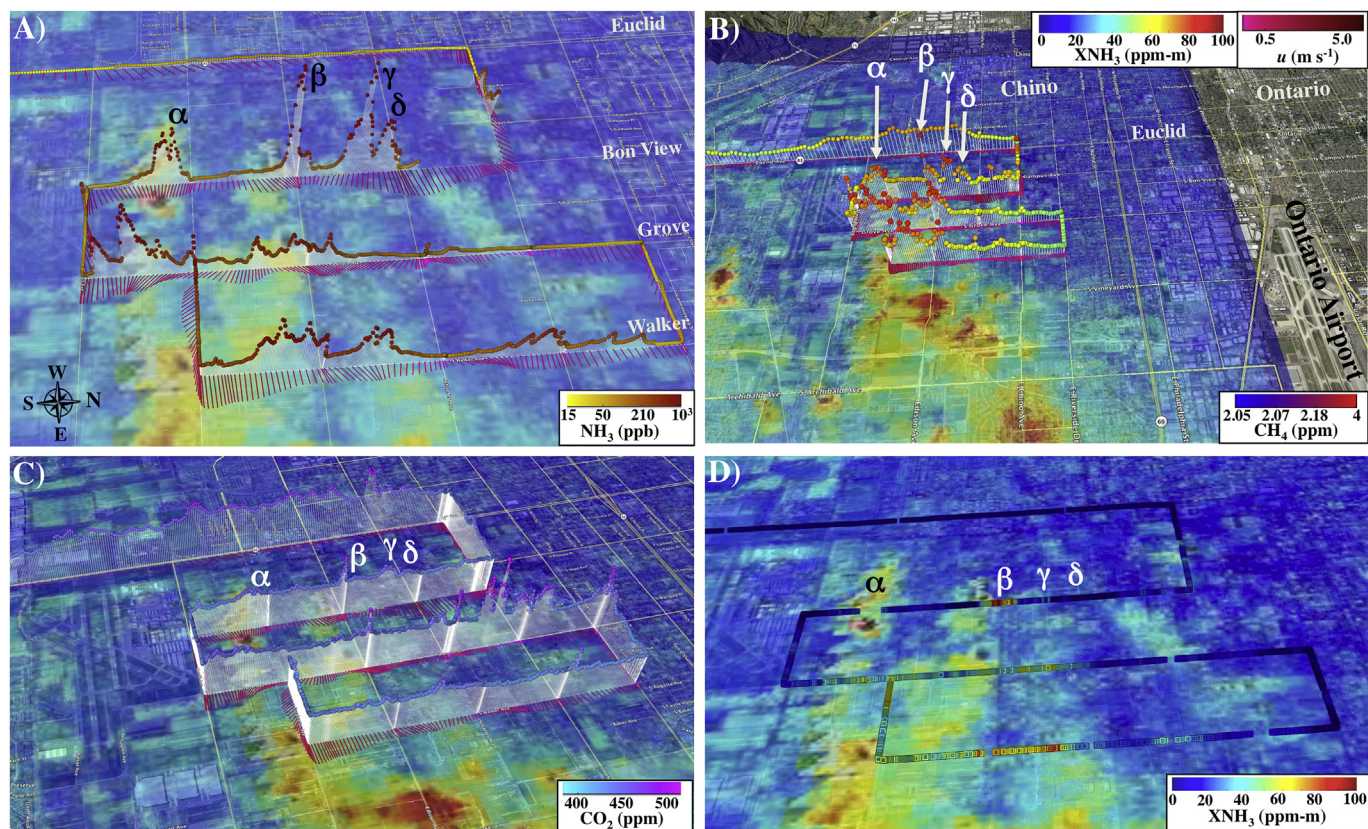
Fig. 7. *In situ* ammonia (NH$_3$) for 25 June 2015, and Mako NH$_3$ column (XNH$_3$)from 25 July 2014. Plumes on Bon View Road labeled. **B)** Wider area view of *in situ* methane (CH$_4$). **C)** *In situ* carbon dioxide (CO$_2$). **D)** MISTIR XNH$_3$. Shown in the Google Earth environment.
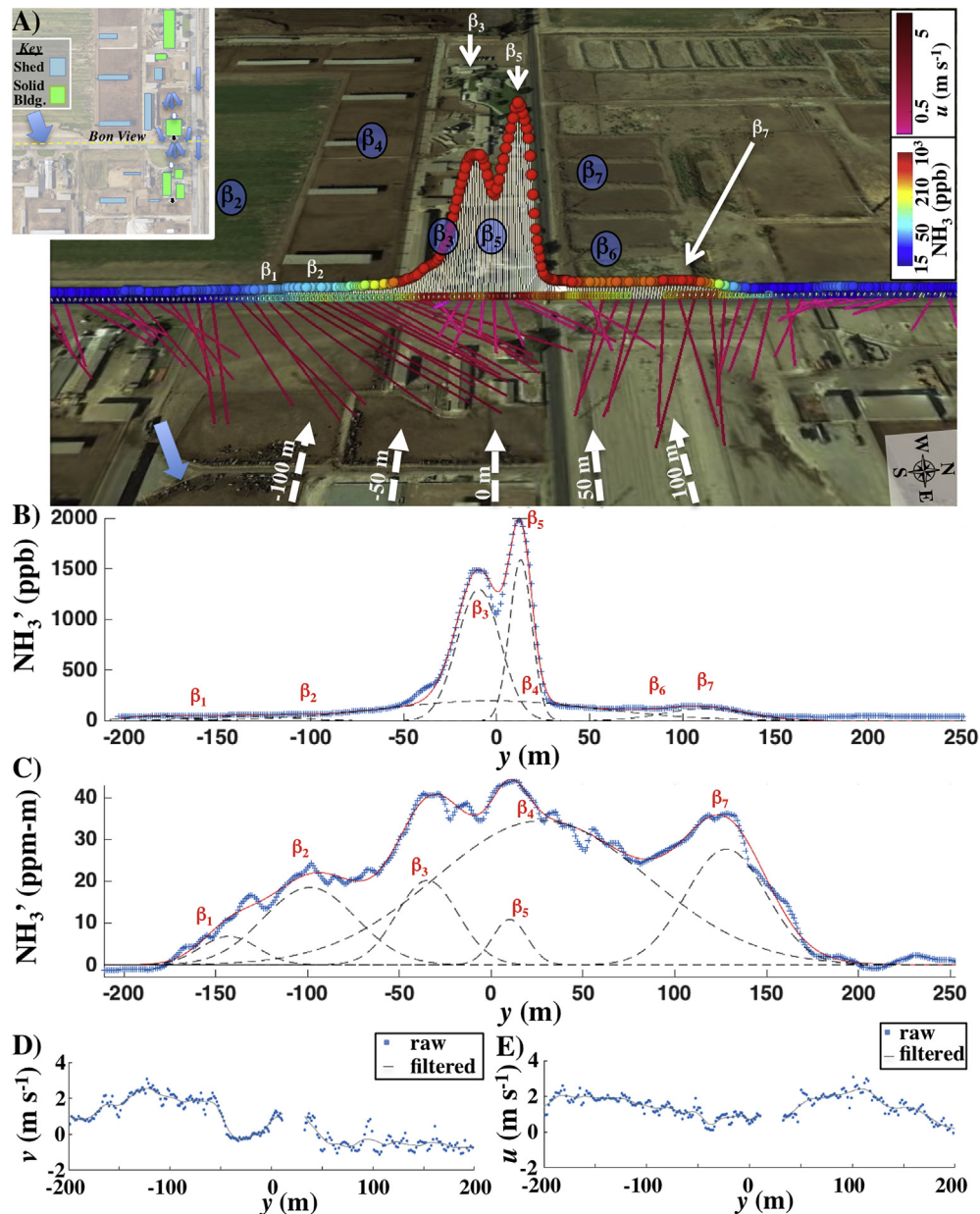
Fig. 8. A) Column ammonia (XNH₃) and *in situ* ammonia (NH₃) and winds (*u*) for dairy β, Bon View Road transit (See Fig. 7), 25 June 2015 in the Google Earth environment. Modeled plume features are labeled with transect origin (*y* = 0) centered on plume β₆, where (*y*) is lateral distance. Locations of 7I model plumes labeled. Inset shows schematic of wind patterns and structures. **B)** AMOG *in situ* NH₃ anomaly (NH₃′) and seven plume informed (7I) model for *y*, **C)** MISTIR XNH₃ anomaly (XNH₃′) and 6U model versus *y*. **D)** Filtered and unfiltered east wind component (*u*) and **E)** north wind component (*v*) with respect to *y*. Wind data gap is from acceleration quality filtering. Data key on figure.
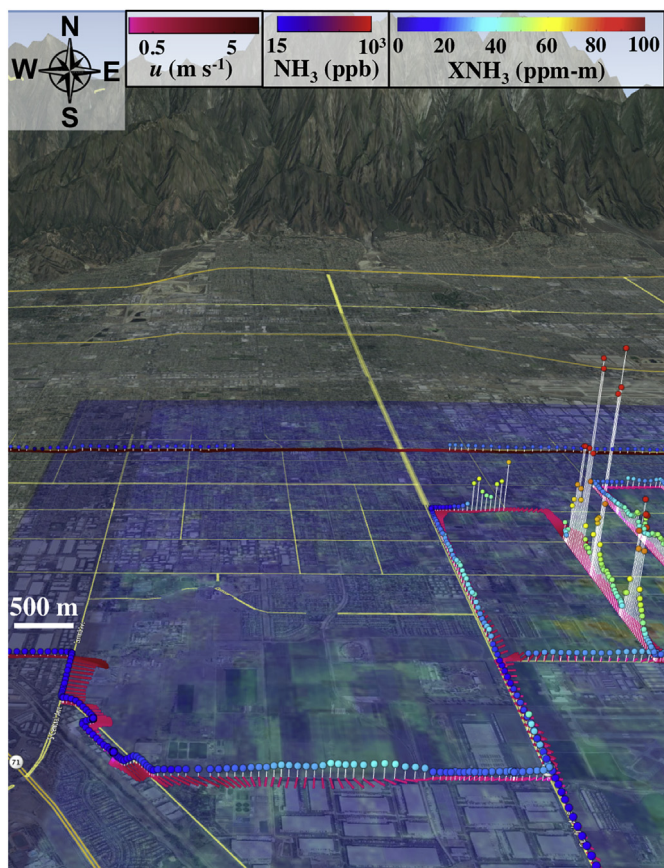
3.2.1.1. Dairy scale emissions.

The AMOG - MISTIR convoy surveyed a number of individual facilities in the Chino Dairy Complex (Fig. 7) including several that exhibited very high NH₃ and XNH₃ values immediately downwind of several Bon View Rd. dairies. NH₃ concentrations to 1869 ppb and XNH₃ columns to 45 ppm-m (plume β) were observed. AMOG also observed strong CH_4 and CO_2 plumes from these dairies. These dairies are amongst the most upwind of the Chino dairies and thus should exhibit minimum confusion from overlapping upwind plumes.

Unfortunately, only data for dairy β allowed a comparison between MISTIR and AMOG due to several data gaps (e.g., plume α, MISTIR, Fig. 7D) and emissions unsteadiness (puffiness) for several dairies. For example, dairy plume δ in AMOG data was not observed by MISTIR. More telling is that although peak AMOG NH₃ for dairies β and γ were comparable, MISTIR only observed a strong NH₃ plume with a comparable width to that of AMOG for plume β, but an orders-of-magnitude weaker plume from dairy γ. Plume γ was evident in Mako data and showed unsteadiness in this dairy's emissions. Given that MISTIR observes column density (observes a plume no matter where overhead it passes), this demonstrates emission variability on the (~20 s) time separating the platforms.

AMOG-MISTIR spatial agreement for dairy β was excellent, albeit with a southward (along-track) displacement of MISTIR relative to AMOG (Fig. 8B versus 8C). This displacement corresponded to observed near-surface wind veering induced by nearby structures.

Near-surface winds were complex for dairy β (Fig. 8B), primarily due to modification by a large, solid, downwind building, ~40 m east of Bon View Road (Fig. 8A) and to a lesser extent by a smaller, solid upwind building ~30 m west of Bon View Road. A clearly

Fig. 9. AMOG ammonia (NH_3) concentration and wind (u) to the southwest of the Chino Dairy Complex, superimposed over Mako column NH_3 (XNH_3). Data key and size scale on figure. Shown in the Google Earth environment.

This represents less than $10°$ of wind veer, i.e., small, albeit slightly larger than for the main plume. This almost certainly arose from the nearby structures that forced these near-surface winds to align with their orientation, i.e., westerly. Overall, the MISTIR XNH_3 shape was very different from AMOG NH_3, suggesting that the two prominent features in the NH_3 *in situ* data (β_3, β_5) are not dominant to overall emissions from this dairy.

Initially, a two-plume uninformed model (β_3, β_5) was considered; however, although the two prominent plume structures are nearly Gaussian, they intercept above background, i.e., ride atop a broad NH_3 feature. Broad features correspond to more distant sources. A three-plume model, though, could not reproduce the weaker plume structures to the north (β_6, β_7) and south (β_1, β_2). These six plumes were even more apparent in the MISTIR data. Thus, a six-plume uninformed (6U) MISTIR model was developed and used to inform a six plume (6I) AMOG NH_3 model (except plume β_4). MISTIR column data are largely insensitive to plume irregularities that arise from the many violations of the Gaussian plume model criteria by these near-field measurements of sources located nearby structures. See Table 3 for dairy β model results.

The 6U MISTIR model showed that the two prominent plume features (β_3, β_5) transported only a combined 20% of the dairy emissions, whereas the broad feature β_4 transported 60%. This is because these features (β_3, β_5) have nearby sources ($D = 80$, 50 m, respectively). By contrast, plume β_4 originated from $D = 300$ m, i.e., from the cowsheds on the distant side of the dairy. Plumes β_1 and β_2 were not significant (2.2, 2.4%) and originated in a large field ($D = 105$, 125 m) as did plume β_7, which contributed only 5% of total emissions.

The MISTIR 6U model informed a six plume (6I) AMOG NH_3 model with widths specified by MISTIR, while the plume center location was allowed to vary. The AMOG 6I model had difficulty with the main plume features (β_3, β_5), which could not be well fit with MISTIR widths, requiring incorporation of a non-unity turbulence constraint factor, k. Incorporation of k moved plumes β_3 and β_5 nearer, but worsened AMOG-MISTIR agreement for plume β_5 for both E and relative contribution. This suggests greater complexity in the effect of flow convergence on turbulence than characterized by a simple k factor. These sources correspond to cowsheds that were aligned with the prevailing winds and clearly were in the near field.

$E_{AMOG}(NH_3)_{6I}$ was 210 Mg yr^{-1}, in fairly close (57%) agreement with E_{MISTIR}, particularly given the indications of puffiness. For the dominant plume β_4, AMOG-MISTIR agreement for E was 66%, similar to the agreement for the overall dairy. The relative importance of plumes β_3 and β_5 was smaller, ~12% combined). AMOG-

divergent wind flow is centered on the downwind buildings that drive a convergence with the overall westerly winds ($x\sim40$ m). This convergence creates notable asymmetry in plume β_5. The emission calculations used $u = 3.1$ m s^{-1} based on the average of the upper 5% of each wind component, which also provided the wind direction. This direction agreed well with winds downwind of the open field shown at $x \sim$ -150 m in Fig. 8B.

The shape of the MISTIR XNH_3 transect suggests the dairy plume's edges were at -175 m and $+175$ m, which corresponded to the width of the AMOG NH_3 feature, albeit with an ~25 m offset.

Table 3
Uninformed and informed CH_4 plume inversion model for the Chino Dairy Complex.

NH_3				NH_3		NH_3				CO_2			CH_4	
6I-AMOG				6U-MISTIR		7I-AMOG				7I-AMOG			7I-AMOG	
#	k	E	D	E	D	k	E	D	R_E	E	D	R_E	E	D
-	-	(Mg yr^{-1})	(m)	(Mg yr^{-1})	(m)	-	(Mg yr^{-1})	(m)	-	(Gg yr^{-1})	(m)	-	(Mg yr^{-1})	(m)
1	1	4	105	11	105	1	3.0	87	2.00	ND	87		2	87
2	1	5	125	47	125	1	3.6	88	2.50	ND	88		2	88
3	0.72	40	80	34	110	0.72	24.6	60	3.33	0.87	60	72.5	12	60
4	1	130	295	198	295	1	67.2	195	3.42	3.90	195	102.6	38	195
5	0.60	20	47	10	70	0.6	18.2	50	1.33	0.93	50	62.0	15	50
6	0	ND				1	0.3	45		0.06	45		1	45
7	1	10	120	61	120	1	19.2	140	0.48	2.48	140	118.1	21	140
Tot		209		361			136		1.50	8.2		90.5	91	
Mean									2.08			89.2		
std									1.08			22.6		

*Model descriptor is NU or NI where N is number of plumes, U − Uninformed, I − Informed, and I-2 − Turbulence optimized. E_{NH3}, E_{CH4}, and E_{CO2} are the ammonia (NH_3), methane (CH_4), and carbon dioxide (CO_2) fluxes, D is distance, and $R_E = E_{NH3}/E_{CH4}$ or E_{CO2}/E_{CH4}.

MISTIR agreement for β_3 was good (within 18%). The MISTIR 6I model estimated plume β_7 was larger by a factor of 6 than from AMOG (6I), 61 Mg yr^{-1} versus 10. Mg yr^{-1}, respectively. This was because the six plume model did not include plume β_6 (see 7I model), which would have re-apportioned flux amongst the more northerly plumes.

AMOG CH$_4$ plume structures were far better defined than NH$_3$ structures, and included a small feature on the main plume's southern flank that clearly was a plume and not "noise." Thus, a 7U CH$_4$ model was developed and applied to inform the AMOG NH$_3$ and CO$_2$ models (7I). This 7I model was developed separately from the 6U MISTIR model to avoid assuming that CH$_4$ and NH$_3$ sources are co-located. MISTIR data suggests a narrower plume β_4, whereas AMOG data suggest a broader plume, i.e., a more distant source. Thus, the initial conditions for β_4 optimization used the AMOG-data derived width.

The AMOG seven-plume, uninformed (7U) CH$_4$ model found E_{AMOG} (CH$_4$)$_{7I}$ = 91 Mg yr^{-1}. This model used the k factors derived for β_3 and β_5 from the AMOG 6U model. Most significantly, the 7I CH$_4$ model found the broad plume (β_4) originated significantly closer ($D = 195$ m), now from the middle of a line of cowsheds oriented approximately along the wind direction (Fig. 8A). This shift of the source closer (and to a more realistic location) decreased the contribution of plume β_4 to 42% of total E_{AMOG} (CH$_4$)$_{7I}$. The combined contribution from plumes β_3 and β_5 was 30%. A seventh, small plume (β_6) was identified that contributed 0.3 Mg yr^{-1}.

The 7U CH$_4$ model was used to inform a seven-plume AMOG (7I) NH$_3$ model. Specifically, plume widths were from the 7U CH$_4$ model, although the plume centers were allowed to vary. Overall agreement with E_{MISTIR} was worse, E_{AMOG} (NH$_3$)$_{7I}$ = 140 Gg yr^{-1} (38% of E_{MISTIR} (NH$_3$)). The relative importance of the dominant plume, β_4, was 49%, in closer agreement with the MISTIR apportionment of 55% and similar to the relative importance of plume β_4 for CH$_4$ (42%). Plumes β_3 and β_5 shifted to closer (60 and 50 m, respectively), with β_5 corresponding to directly behind the house, where one Google Earth timeline image showed cows congregating, perhaps for feed. Agreement was worse between E_{AMOG} and E_{MISTIR} for plume β_4, which is unsurprising as this was the main difference between the 7U and 6I NH$_3$ models and for plume β_7 (from 16% to 31%).

AMOG-MISTIR agreement was better for all other plumes, in some cases significantly. Plumes β_3 and β_5 were more important, contributing a combined 31% of the plume (compared to 12% from MISTIR). This was very similar to their contribution to the overall CH$_4$ plume (30%). Application of the 7I AMOG CH$_4$ model to CO$_2$ yielded 8.2 Gg yr^{-1}, with CO$_2$ emissions for dairy β also dominated by plume β_4 (47% of E_{AMOG} (CO$_2$)$_{7I}$). Plume β_7 was significantly more important to overall CO$_2$ emissions, contributing 30%.

Based on E_{AMOG} (NH$_3$)$_{7I}$, E_{AMOG} (CO$_2$)$_{7U}$, and E_{AMOG} (CH$_4$)$_{7I}$ and emission factors of 55, 4400, and 53 kg cow^{-1} yr^{-1} (Kinsman et al., 1995; Leytem et al., 2011; Peischl et al., 2013), a total of 2480, 1870, and 1720 cows (average 2020 cows), respectively, were estimated. In the literature, these emission factors lie within broad ranges, thus the emission factors were harmonized (61, 4080, and 45 kg cow^{-1} yr^{-1} for NH$_3$, CO$_2$, and CH$_4$) to a 2020 cowherd size to explore sub-facility differences between the larger plumes. Specifically, this analysis looks at emission factors (i.e., predicted cows) that are distinctly different between plumes and thus likely related to husbandry practices.

For the dominant plume β_4, predicted cows are 1100, 960, and 840 for NH$_3$, CO$_2$, and CH$_4$, respectively, i.e., predicted herd sizes agreed within 10%, and the R_E for NH$_3$/CH$_4$ was amongst the highest of all plumes, suggesting greater relative importance of waste emissions over enteric emissions than other plumes. The near field plume β_3, which originated from a cow shed, similarly showed

relatively enhanced NH$_3$ compared to CO$_2$ and CH$_4$; 400, 210, and 270 predicted cows, respectively.

For plume β_5, which originated behind a house in an open yard with no cowsheds, the pattern was different with lower NH$_3$ emissions relative to CO$_2$ and CH$_4$ and estimated herd sizes of 300, 230, and 330 cows for NH$_3$, CO$_2$, and CH$_4$, respectively. The difference in NH$_3$ enhancement over CH$_4$ between the cow shed plumes and the open yard plume is consistent with sheds enhancing NH$_3$ formation over CH$_4$. These emission factors appear to be too low by almost an order of magnitude — manual analysis of 15 Google Earth images from Dec. 2003 to Oct. 2016 of the 50×50 m cow yard behind the house showed the average number of cows was 32 ± 13 cows. The AMOG inversion suggested the plume originated immediately behind the house. In contrast, Google Earth timeline imagery suggested cows primarily congregate near the far fence where feeding likely occurs (85 m); in only one of the images were cows near the house. MISTIR suggested the plume originated at 70 m, directly in the cow yard's center. The similarity in the estimated number of cows based on emission factors from the three gases, the similar overestimate, and the centralized source location, could reflect legacy emissions from soil caused by manure deposited over the years. The house clearly induced additional mixing that AMOG interpreted as a nearer source, whereas the MISTIR source location is appropriate for legacy emissions and is closer to where the cows generally congregated. Other plumes could not be analyzed in this manner as the cowsheds obscured the number of cows in Google Earth imagery.

Finally, plume β_7 showed a significantly different pattern; 310, 610, and 470 predicted cows for NH$_3$, CO$_2$, and CH$_4$, respectively. Plume β_7 likely originated in one of the upwind solid structures, with high CO$_2$ suggesting a combustion-related source. Other plumes were small, implying very few cows — and might represent waste emissions rather than combined ruminant-waste emissions.

There were similarities in the relative strengths of different sub-facility plumes for the three gases. For example, plume β_4 contributed 50%, 43%, and 47%, of E_{AMOG} (NH$_3$)$_{7I}$, E_{AMOG} (CH$_4$)$_{7U}$, and E_{AMOG} (CO$_2$)$_{7I}$, respectively, whereas the combined contributions from plumes β_3 and β_5 was 31%, 30%, and 22%, respectively for these gases.

Overall R_E for NH$_3$/CH$_4$ for dairy β was 1.50, significantly different from that for the overall Chino plume ($R_E = 0.49$) or the plumes derived from the overall Chino plumes ($0.20 < R_{E-NH3} < 0.93$). R_{E-NH3} is the ratio of E_{NH3} to E_{CH4}, with CH$_4$ chosen as the denominator because CH$_4$ includes waste and animal emissions whereas NH$_3$ is primarily waste derived. CO$_2$ is similar to CH$_4$ in that it comes from both animals and waste; however, CO$_2$ also arises from mechanized dairy activities related to internal combustion. Given the small herd size of dairy β and the small contribution it made to the overall plume (~2.2% based on MISTIR data), R_{E-NH3} for dairy β would have negligible impact on R_{E-NH3} for the overall Chino Dairy plume. This suggests practices at dairy β are distinct from the other dairies that dominated the overall plume emissions.

R_{E-CO2} for dairy β was 91; however, this was skewed due to plume β_7, for which $R_{E-CO2} = 118$, whereas the three other plumes for which CO$_2$ emissions could be derived were between 62 and 103. This strongly suggests plume β_7 included a significant dairy infrastructure contribution. R_{E-CH4} for plume β_7 also was significantly different from other plumes, suggesting natural gas combustion such as from a heater, consistent with origination in a structure. Plume β_7 contributed a significant fraction of the dairy NH$_3$ emissions, suggesting emissions also included cows.

3.3. Agricultural field emissions

Husbandry generates significant waste, which often is used to

fertilize nearby fields, leading these fields to be an emissions source. For example, Mako XNH_3 was enhanced above a number of agricultural fields to the west of the Chino Dairy Complex (Fig. 9). The downwind plume from these agricultural field emissions was captured clearly in AMOG NH_3 data. AMOG plume dimensions and those of the Mako enhanced NH_3 columns match, as do their spatial structures. These area emissions also are observed in Mako data for suburban communities to the southeast of Chino, where dairies were historically; however, similar enhancements are completely lacking from communities to the northwest where there was no historical husbandry legacy (Fig. 5B). Deriving emissions from these agricultural fields is beyond this study's scope.

3.4. Seasonality

Husbandry NH_3 emissions arise both from animals and from the husbandry environment, which are well documented to exhibit seasonal variations due to chemistry (evaporation and bi-directional conversion with ammonium aerosol) and microbial production, which is strongly temperature dependent (Sutton et al., 2013). Seasonal trends in IASI XNH_3 and XCH_4 and major meteorology drivers were compared to explore the importance of meteorological forcing. Specifically, monthly IASI satellite morning overpass (18:00 GMT) downwind XNH_3 (Van Damme et al., 2017; Whitburn et al., 2016) for (33.8—34.3°N, 117—118°W) were normalized for each year 2008—2016 and then the monthly-normalized, averaged column-NH_3 (XNH_{3-N}) was derived for the dataset.

Husbandry CH_4 emissions arise from animals and waste, with the latter depending on the environment. Unlike NH_3, for which Chino is the largest Los Angeles Basin source, CH_4 has many other basin sources, particularly along the Pacific coast where large, active oil and gas fields are located (Peischl et al., 2013). Thus, the IASI XCH_4 anomaly (XCH_4') seasonal trend was calculated by comparing IASI XCH_4 for a downwind and a reference box, 33.8—34.1°N, 117—117.6°W and 34.05—34.3°N, 117—118°W, respectively (Fig. 3). For reference, Chino is at 34.0°N, 117.6°W. These boxes were selected based on the gridded average lower 4-km XCH_4 from IASI for 2010—2016. An upwind (west) reference box was not used because of orography (Chino Hills) and because air from west Orange County only partially flows over Chino.

Seasonal trends in annually normalized morning wind speed (u_{n-AM}) were calculated for u 2-h prior to the morning overpass in the same manner. Seasonal temperature was not normalized, but was calculated for 3 h prior to the overpass (T_{AM}). Meteorology data were from MESONET (2017). See Supplemental Figure S7 for seasonal trends that are not normalized. Since our study was investigating seasonal, not monthly, trends, a 3-month running average smoothing filter was applied to all trends.

IASI XNH_3 showed a very strong seasonal variation of almost an order of magnitude with the lowest values in December, and the highest in July (Fig. 10). Some of this variation arises from wind speed, which dilutes the pixels. u_{n-AM} thus could be considered a rough ventilation index that was strongest in spring and weakest in August; however, the seasonal variation with respect to ventilation varies little (<10%) over most of the year (mid-May to mid-March), except April—May when it is elevated by ~40%. Thus, ventilation, whose impact is close to linear, shows a different seasonal trend and too small a magnitude to explain the seasonal XNH_3 variation. T_{AM} shows a similar trend to XNH_3, increasing from December to July and decreasing from September to December. There appears to be a slight offset between IASI XNH_3 and T_{AM}, which remains fairly constant from July—September. Some of this difference likely relates to the decreasing trend in u_{n-AM} from May through October. Other differences could relate to seasonal practice differences, although a review of Chino husbandry practices suggests not.
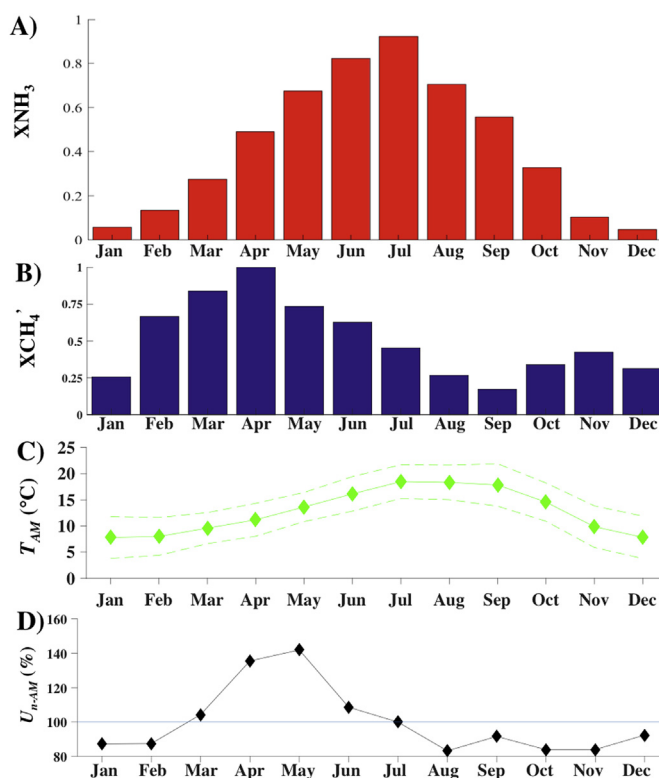

Fig. 10. IASI normalized, monthly-averaged, morning overpass A) 2008—2016 full atmosphere, Chino downwind column ammonia (XNH_3) and B) 2010—2016, lower 4 km delta column methane (ΔXCH_4) relative to reference box (Fig. 3B). C) Morning temperature (T_{AM}) for 1600—1800 UTC and D) normalized wind deviation from annual average (u_{n-AM}). See Supp. Fig. S7 for non-normalized data.

Although lower thermal contrast reduces IASI winter sensitivity, this is unlikely to affect the seasonal XNH_3 trend given the XNH_3 signal strength.

ΔXCH_4 between the downwind and reference boxes was ~4.6 ppb, and exhibited about half the seasonal trend of XNH_3 (~400%), with a peak in April and a second peak in November. Since this corresponds to peak winds, the emissions trend is greater, perhaps about half given the trend in wind speed. The ΔXCH_4 seasonal trend is unexpected as it is inversely related to temperature. There is a loose correlation with wind speed, thus transport could potentially explain some of the difference. However, these two periods do correspond to seasonal waste scraping and removal, which occurs before and after seasonal winter rains (CDFA, personal communication, 2018). In contrast, there is good temporal agreement between the CH_4 seasonal trend and milk production (Supplemental Fig. S3).

4. Discussion

4.1. Experimental design and mobile surface measurements

To provide useful information for emissions derivation, stationary sites must be well positioned downwind of sources that are steady, and winds must be predominantly prevailing. For unsteady sources, stationary measurements cannot discriminate between temporal variability that arises from transport and from unsteady emissions. Mobile measurements address these issues by ensuring data are collected downwind based on real-time determination of the wind frame of reference. Additionally, mobile measurements provide a snapshot of emissions, separating temporal and transport

variability.

Similarly, airborne imaging spectroscopy provides an area snapshot that characterizes transport variability from turbulence, emission unsteadiness, and source spatial heterogeneity on a range of scales. In fact, Mako airborne imaging spectrometry captures a short time-history of emissions providing evidence of emissions unsteadiness and puffiness during transport. Several possible mechanisms could underlie the observed unsteady emissions, one of which may relate to periodic ventilation of the air under cowshed roofs where emitted gases can accumulate (from personal nasal observations) by turbulence and winds.

Mobile *in situ* measurements are extremely sensitive for a wide range of gases compared to airborne remote sensing, but provide at best an incomplete context. Hence the experimental design was multi-grid, combining ultrasensitive *in situ* mobile data with airborne remote sensing that swath-mapped the entire area. Logistics of airborne data collection are far more challenging than mobile surface, thus mobile surface remote sensing (MISTIR) data were collected with mobile *in situ* data to address in part the time gap with the airborne data. The experimental design developed a real-time characterization of the wind flow across the Chino Dairy Complex to confirm the planned mobile measurement strategy. For example, if the winds had been more southerly, say from 230°, the plume would have intercepted the SR-60/I-15 intersection. In such a case, the survey would have continued east on SR-60 until the plume was completely transited, followed by a return to the intersection, and then the collection of a long south-north transit, also completely crossing the plume.

Most importantly, mobile *in situ* data can be collected downwind of the wide diversity of husbandry emission sources, either on access roads or public (more distant) roads. Although long-distance open path analyzers provide a significant improvement over stationary *in situ* analyzers — they do not observe where the plume crosses the beam, thus segregating emissions between distinct sources can be difficult to impossible.

In situ NH_3 measurements are challenging due to its stickiness. Agreement with the remote sensing derived emissions, which suffer no latency from gas stickiness, demonstrated the significant improvement in AMOG NH_3 data from the flow-path design improvements in Leifer et al. (2016a,b,c).

The experimental design included satellite data analysis to understand the seasonality in emissions. Both NH_3 and CH_4 emissions are strongly temperature dependent on daily and seasonal time scales (Leytem et al., 2011). In the case of CH_4, this is due to microbial degradation of manure, and thus depends on the manure storage manner — large piles tend to thermally self-regulate. NH_3 volatilization and bi-directional conversion between ammonium salt aerosol and NH_3 gas also are temperature sensitive, varying seasonally (Stelson and Seinfeld, 1982). Thus, satellite data can allow incorporation of expected seasonal differences for comparisons between campaigns during different seasons (same time of day) for husbandry as discussed herein, but also other sources that exhibit seasonality, for example natural gas and oil production (due to maintenance schedules and seasonal price/demand cycles).

4.2. Real time data visualization

AMOG features real-time data integration and visualization in the Google Earth environment of up to five variables stretching back ~5 min, and a 40-min time history for a dozen trace gases. For husbandry emissions, winds, CH_4 and NH_3 are real-time visualized to provide wind flow-field feedback to the operator, allowing a rough estimation of source(s) and their strength. The time history shows recent significant anomalies that may not have been noted when traversed. MISTIR also provides a real-time display of the detected gases time history and their approximate strengths.

However, first looks can be deceptive. The real-time visualizations suggested the individual dairy plume was well characterized by two approximately Gaussian plumes. Instead, inversion modeling revealed greater complexity and would have benefitted greatly from multiple passes instead of the single pass.

The inversion model was robust for emissions derivation and identifying a reasonable number of sources. In part this arises from careful wind measurement, note that Eqn. (1) is linear with concentration but highly non-linear with wind speed and direction. In contrast, the model had trouble for a number of situations in deriving the location of sources and also apportionment of flux between different sources. Specific issues arise in the interpretation of small-scale features as real, nearby sources or noise (variability induced by wind flow heterogeneity). However, nearby small sources are weak and thus interpretation errors are not significant to overall emissions characterization. Multiple passes would have improved the analysis, identifying persistent sources that were not the result of turbulence or puffy emissions. Additionally, where flow-field heterogeneity induces non-Gaussian trends in the plume transect, additional passes are needed to optimize between controlling parameters including wind speed, turbulence scales, distance, and strength.

Interpretation of the plume from the Chino Dairy Complex and the dairy on Bon View Road was complicated by numerous sources that spanned a range of strengths and spatial distributions (observed in the Mako data). Even interpretation of Mako data is challenged by the plumes over-riding numerous downwind sources and temporal variability (puffiness) in plume emissions. Overall, the inversion was successful at identifying the nearest plume and the largest plume, but completely unsuccessful at identifying plumes behind a large plume, i.e., shadow masking. For example, Plume P6 (Fig. 5) shadowed the more distant dairies evident in the Mako data, some of which were surveyed (e.g., Plume α, Fig. 7). Although the shadowed plumes do contribute additively to the transect data, the resulting deviations from Gaussian shape cannot be separated from either noise due to wind field variability and/or cannot produce a unique solution, i.e., an infinite combination of more distant plumes could yield the same observed data. To some extent, transect repetition could improve interpretation, particularly if winds shift significantly. However, Chino area winds are strongly controlled by orography and thus are predominantly prevailing (Fig. 2B), i.e., unlikely to shift significantly.

Additionally, real-time data visualization between multiple platforms by for example, mirroring on a server to which both platforms were subscribed, would have identified the MISTIR data gap that occurred in the middle of plume α, or highlighted the absence of an observed plume in MISTIR data where AMOG had observed a strong plume only 20 s earlier. In both cases, this would have prompted repeat transits once the operators noted the unsteadiness of emissions.

4.3. Near-field inversion challenges and limitations

The Gaussian plume model was developed for conditions that were violated multiply by the near-dairy field surveys. Specifically, the wind field must be homogeneous, which requires an absence of physical structures in the near field (upwind and downwind of the survey transect). This is because structures create convergence and divergence flows (e.g., Fig. 8). Flow-field heterogeneity was the reason the Gaussian plume model failed to converge for plumes β_3 and β_5, which originated from nearer than 100 m. These plumes were modeled by including a turbulence constraint factor (k) which Leifer et al. (2016a) developed to account for orographic constraints on turbulence growth and thus lateral transport, an effect that is

similar to wind-field convergence. This likely was more pronounced for these near-field plumes where a significant fraction of the plume is still close to the surface where wind heterogeneity is greatest.

Briggs (1973) suggests an exponent of $(+0.5)$ for the near-field turbulence parameterization for slightly unstable conditions to account for the fact that the plume primarily is at low altitude where surface winds are weaker. However, an attempt to use a $+0.5$ exponent in the inversion model failed to reproduce the observed plume transect data. We propose this failure arises because of enhanced vertical transport driven by the vertical winds that enhance vertical mixing and arises from convergence in the 2D surface winds. By continuity, this convergence must drive vertical winds. This is equivalent to spatially varying roughness elements along the plume advection path, constituting another plume model violation. The k factor was developed in Leifer et al. (2016a) to address the effect of orography (canyon walls) that constrained the 2D dispersion of winds, and thus does not address vertical motions. To develop a k factor that addresses vertical mixing, AMOG Surveyor has been upgraded with a 3D sonic anemometer (Model 81,000, Campbell Scientific, UT). MISTIR column fluxes are derived without reference to turbulence parameterizations.

The foregoing discussion was for the wind field in the (y-z) plane of the survey transect, but the 3-D wind field also varies along the path between the source and survey transect. The Gaussian plume model assumes a homogeneous wind field. Wind flow-field heterogeneity was modeled by a k factor that accounts for these non-homogeneities integrated over the plume flight, but only was applied to the 2D turbulence. Agreement was good for β_3 (72%) and poor for β_5 (180%) for which k was 0.72 and 0.60, respectively. The closer k is to unity, the less impact that flow field heterogeneity has on the plume. A value of k of 0.60 indicates fairly strong turbulence constraint. The lower k and poorer agreement occurred on the lee side of the structures, rather than the upwind side, where greater flow field distortions would be expected. Collection of additional transects would provide further insights into improved estimation and treatment of k.

The Gaussian plume model assumes steady emissions. In contrast, comparison of AMOG and MISTIR data suggests unsteady (puffy) emissions, confirmed in Mako airborne remote sensing data. For some dairies, AMOG observed very strong plumes, while MISTIR observed none (separation was ~5—20 s) and vice versa. In the case of dairy β (Fig. 7), where both MISTIR and AMOG showed strong plumes, good agreement (66%) was found between MISTIR and AMOG. Although a hands-free radio was used for communication between platforms, this puffiness was not noted. The simple solution (with hindsight) would have been multiple transect repetitions to allow for more opportunities to observe this behavior. Unsteady emissions were not an issue for the far field I-15 transit. This likely was from turbulence mixing in the wind direction during transport from the source to the transect, which smoothes out puffiness for the different sources.

Interpretation was complicated by the numerous sources revealed in Mako data and also the interior Chino Dairy surveys that could not be disentangled from a single transect. However, additional transects would only have improved the analysis marginally because winds are typically prevailing and co-aligned with roads and dairies. This leads to nearer plumes shadowing or masking more distant plumes. Specifically, the additive signature cannot be discriminated from noise or variability induced by the wind field, and moreover, the more distant plumes are not uniquely defined.

In principle, emission variability could have interfered with the main Chino Dairy complex plume inversion. However, the excellent AMOG-MISTIR agreement for the main dairy plume in the far field,

relative to the difficulty in the near field from unsteady emissions, suggests that diffusion (along-wind and cross-wind) largely has reduced the impact on the transect data from unsteadiness. Although repeat transects to characterize emissions for wind shifts would provide additional information, Chino winds are generally prevailing, thus the sole solution is surveys within the dairy complex. However, surveys in the interior of the Chino Dairy Complex would be in these dairies near-field. As noted, emissions variability prevented intercomparison between MISTIR and AMOG for many dairies. Unsteadiness of emissions only can be addressed by repeat surveys, even for airborne remote sensing data.

4.4. Informed versus uninformed model

The informed inversion models showed significant improvements over uninformed models. In the uninformed model, only information from a single transect downwind of the Chino Dairy Complex was used to derive emissions. This initial uninformed (2U) model performed poorly, suggesting emissions that were ~200% of the reference MISTIR NH_3 flux with very poor source attribution. The informed NH_3 models incorporated *in situ* CH_4 data and airborne remote sensing data to aid in specifying the number of plumes to model. The 6I informed model did not specify the source origins, which were derived from the fit. Agreement was much better, within 9% of MISTIR, and source locations were better inferred, as defined by originating from dairies and in particular active dairies observed in airborne remote sensing data. Further refinement (8I) allowed one observed plume to originate from four sources (as suggested by remote sensing data) and used CH_4 plume widths (CH_4 does not exhibit latency) in an informed NH_3 model, improving AMOG-MISTIR agreement to within ~5%, and much improved the location of plume sources proximal to dairies. This model refinement illustrated the shadowing problem, discussed in section 4.3.

As noted, this study showed how the plume inversion is improved by combining information from different gases. A second finding is that remote sensing data of a gas with a strong signal (e.g., NH_3) can be leveraged to improve inversions of both the primary gas (NH_3), by better assessing the number of sources, and also of a second, associated gas (CH_4). This was true even though a year separated the *in situ* data and the airborne data. Airborne remote sensing is significantly more expensive and logistically complicated than surface mobile observations. Thus, fusion of the two provides significant benefits, for example, surface mobile *in situ* surveys can be collected frequently, using infrequent airborne remote sensing and/or mobile surface *in situ* data to inform source locations. Such data fusion allows repeat surface mobile data to build up a statistical picture of emissions based upon improved source location from remote sensing.

4.5. Husbandry emissions seasonal variability

Given the dependency of husbandry NH_3 and CH_4 emissions on weather, particularly temperature, it is unsurprising that emissions exhibit seasonality. Satellite data have mapped hemispheric-scale seasonal variations of 150% in northern hemisphere AIRS NH_3 data (Warner et al., 2016), much less than observed for the Chino Dairy Complex (Fig. 10A). However, hemispheric-scale data combine emissions from non-husbandry fertilizer application with husbandry and biomass burning. Moreover, fertilizer application times and temperature trends vary strongly across the northern hemisphere, smoothing and reducing seasonality.

This study focused on the Chino Dairy Complex, which is an isolated NH_3 source in the Los Angeles Basin, and documented a clear NH_3 seasonal variation of approximately a factor of 10. A

smaller, but still highly significant variation of ~400% was found for CH_4 (Fig. 10B). For CH_4, the presence of other basin sources such as landfills and hydrocarbon production and natural gas distribution obscures the husbandry seasonality. Winds were uncorrelated with the NH_3 trend and positively correlated (amplifying) with the CH_4 trend, thus dilution cannot explain the seasonal variations. Transport could explain some (40%) of the seasonal CH_4 variation due to advection; however, the few sources (landfills) that are upwind under prevailing winds are tens of kilometers distant. Prevailing winds transport oil and gas CH_4 emissions from the western Los Angeles Basin bypassing Chino to the north. Additionally, landfill seasonality is weaker, amounting to a factor of two in an area where precipitation plays a role (Chanton and Liptay, 2000) in part from greater microbial generation and also loss in the warmer seasons. Additionally, emissions from the nearest upwind landfill — the Olinda Alpha Landfill - resulted primarily from earthmoving operation disturbances with annualized inventory emissions of 11 Gg yr^{-1} (Krautwurst et al., 2016). This is a third of the Dairy Complex's output and thus too small to drive the observed variation. Additionally, Olinda emissions were for disturbance conditions, which are not continuous — e.g., weekends and other times. Note that IASI column measurements are independent of PBL depth. NH_3 lifetime cannot explain these trends - atmospheric NH_3 lifetimes are hours to days, and thus affect concentrations beyond the study area, e.g., Palm Springs (Leifer et al., 2016b). Moreover, this close to the source, the plume is mostly NH_3, not NH_4 aerosols (Nowak et al., 2012), thus the bidirectional temperature dependent transformation between the gas and aerosol phases in the atmosphere (Dawson et al., 2007) cannot underlie the seasonal variation. Wet deposition in Southern California is insignificant due to arid climate and infrequent precipitation, although seasonal rains should amplify seasonal patterns elsewhere such as in the tropics.

Many factors contribute to NH_3 and CH_4 seasonality, particularly emissions from microbial processes in waste that increase strongly with temperature, as well as NH_3 volatilization (Bussink and Oenema, 1998) and the conversion of NH_4 salts in waste to NH_3. Similarly, for the far more extreme climate in Idaho, Leytem et al. (2011) observed for a 10,000 head farm, diel variations of NH_3 and CH_4 from open lot areas (which dominated emissions) and a waste pond of factors of 3 and 4, respectively. Leytem et al. (2011) reported for ten 2—3 day campaigns spaced across the year, and did not find a clear seasonality in the highly variable data, likely due to sensitivity to wind direction. Harper et al. (2009) found seasonal NH_3 variations of a factor of 10 for three farms ranging from 900 to 1860 cows. As lagoons and yards froze in winter (zero emissions) but contributed two thirds of summer emissions, this study shares little in common with Chino dairies, where wet waste management is not used (Google Earth imagery shows at most one lagoon). Amon et al. (2001) used an open-mesh chamber approach for a 12-cow German dairy and found a winter-to-summer difference of ~12 °C in the interior temperature of stacked manure piles. This corresponded to a factor of 2 higher summer manure CH_4 emissions. The IASI summer-winter NH_3 difference was approximately a factor of ten. This strongly highlights the value of the synoptic and continuous data that can be collected by satellite observation.

In addition to seasonality in waste emissions, enteric CH_4 emissions correlate with animal activity, which is reduced at higher air temperatures, leading Ngwabie et al. (2011) to propose it as a factor that contributes to seasonal trends. Ngwabie et al. (2011) found that animal activity also generally followed the feeding schedule driven in part by daily cycles. Thus, waste production related to higher feed consumption may underlie this relationship This is consistent with Bougouin et al. (2016) data indicating that barn NH_3 emissions increase with outside temperature. Amon et al. (2001) also found diel stall CH_4 emissions variations of ~80% that closely tracked the feeding schedule.

Real world dairies (unlike chamber studies) exhibit variations due to "management practices" that require whole-farm evaluation (McGinn et al., 2006). Real world refers to the actual implementation of husbandry practices, which can deviate from theoretical or intended practices. Management practices can include the number of animals, feed quantity and quality, animal location(s), e.g., in barns or corrals, and waste management. These management practices affect enteric emissions and, by affecting the composition and quantity of waste, waste emissions. Additionally, herd size can change dramatically with seasons — Harper et al. (2009) report on a farm that increased herd size 70% (to 2800) from winter to summer, while only increasing daily nitrogen feed (for the whole farm) by 20%. Timing and stage of lactation, also affects seasonal enteric emissions (Garnsworthy et al., 2012).

Chino dairies use dry manure management for which Sommer and Hutchings (2001) report 50% of NH_3 emissions occur during the first 24 h; however, this is highly temperature sensitive and depends on the ability of NH_3 to infiltrate the soil. Therefore, the frequency of manure removal is important. For Chino diaries, it tends to occur both prior to and after the seasonal winter rains, i.e., it does not match the observed seasonal XNH_3 trend, although it does match the XCH_4 trend. The importance of excess feed to NH_3 emissions was illustrated by Bussink and Oenema (1998) who found higher NH_3 emissions in cooler spring compared to warmer fall, which they attributed to higher springtime nitrogen dietary input. Although feed for the Chino dairies is primarily alfalfa year round due to poor access to silage, milk production is higher in spring, correlating with higher XCH_4. Higher production cows are given access to grain with higher protein levels than alfalfa hay (Peterson, 2000). Higher milk production likely correlates to increased feed, increased waste production, and hence increased CH_4 emissions. This seasonality is despite the cows being on a 12—13 month production cycle that has minimized natural trends associated with spring calving, to reduce milk production being unsynchronized with prices (Supplemental Section S2).

As noted, a strong and smooth seasonal trend was revealed in the synoptic and "rich" satellite data, i.e., it incorporates a statistically large number of dairies and cows spanning over 2000 days. The seasonal NH_3 variation was factor of ten, far higher than reported literature seasonal trends (absent freezing lagoons). Neither winds nor transport nor husbandry practices can explain this variation. Thus, we propose legacy soil emissions underlie this variation.

Specifically, we propose that the cumulative effect of nearly a century of husbandry (Leifer et al., 2016c) led to accumulation of NH_3 and NH_4 salts in soils, which responds to seasonal temperature trends. Where manure is used as fertilizer on fields, emissions of NH_3, (Fig. 9), CH_4, and CO_2 are observed; although in a review, Montes et al. (2013) suggests rapid decrease over a few days, followed by slower decrease based in part on controlled application to pasture land (Sherlock et al., 2002). The NH_3 plume in Fig. 9 for Mako (25 July) and in AMOG and MISTIR data (25 June) do not correspond to fertilizer applications (spring), strongly indicating significantly longer timescales. These results likely are caused by repeated fertilizer applications leading to accumulation of NH_4^+ salts in soils that slowly dissociate and volatilize, particularly in warmer weather. The presence of CH_4 emissions (AMOG) also suggests that organic material buildup and microbial conversion to CH_4 is larger than microbial CH_4 oxidation (Montes et al., 2013).

Supporting this interpretation are the Mako airborne data showing NH_3 emissions from extensive subdivisions to the south and east of Chino - land that supported dairies until recent years, but not from subdivisions to the northwest (Fig. 5) that have not been agricultural for many decades. Conversion from agriculture to

dense urbanization began around 2000 (based on Google Earth timeline imagery), suggesting that legacy emissions persist on decadal time scales. These emissions were evident in the MISTIR and AMOG data (Fig. 6) but were not analyzed as they derive from an extensive dispersed area source and thus are not amenable to a Gaussian plume modeling approach. Nevertheless, they likely are comparable to the overall Chino Dairy Complex emissions in summer to explain the additional significant factor in the seasonal variation above literature expectations. Importantly, these emissions do not reflect the estimated current herd size as used in inventories, but persistent legacy emissions, and are consistent with NH_3 emission factors that are higher than reported (Hristov et al., 2011).

The seasonal variation has important implications for intercomparison of emissions between surveys in different seasons. Assuming that the emissions measured are representative for each season, agreement would not be expected between surveys in different seasons. Thus, Chino Dairy emissions reported here for summer were 30 Gg yr^{-1} CH_4 and 15.7 Gg yr^{-1} NH_3 and represent late morning emissions (as does IASI). This contrasts with October 2014 emissions first reported by Leifer et al. (2016b), which were recalculated using the improved algorithms of this study at 40. Gg CH_4 yr^{-1} and 8.6 Gg NH_3 yr^{-1}. Unfortunately, the 2014 data found most of its emissions from a single source, which in reality arose from multiple nearby and aligned sources that could not be discriminated. As such, actual 2014 fall emissions likely were significantly lower based on this study's findings that underestimating the number of plumes leads to emissions overestimation.

Peischl et al. (2013) interpreted CARB (California Air Resources Board) inventories to imply 31 Gg CH_4 yr^{-1}, and estimated emissions from their late May-early June field data ranging from 24 ± 12 to 88 ± 44 Gg CH_4 yr^{-1}. The seasonal satellite variation in this study suggests an ~33% decrease in CH_4 emissions from May to July (Fig. 9B) with enhanced XCH_4 during time periods of the year when manure is scraped and removed. Given that the number of cows decreased from 55,000 to 45,000 over this period, this study suggests higher annualized emissions in 2013.

For the same campaign, Nowak et al. (2012) estimated 12 ± 4 to 64 ± 30 Gg NH_3 yr^{-1}. The upper estimate is difficult to reconcile with likely emission factors for dry manure management.

Viatte et al. (2017) derived January CH_4 emissions that were half those of Peischl et al. (2013), ascribed to a decreasing number of cows; however, they failed to discuss the effect of seasonality, given that their study was in a different season. Moreover, the number of cows had not decreased by a factor of 2, only ~20%. The IASI nineyear observation (Fig. 10) strongly suggests seasonal variations are driving this discrepancy. Additionally, Viatte et al. (2017) used numerical inversion and ascribed most emissions to lagoons, although no significant lagoon source was found in Mako remote sensing data in 2014 (or in following years) or Google Earth imagery, nor for the plumes mapped in this study.

4.6. Dairy practices

Husbandry gases of concern are emitted both from enteric activity and waste and farm infrastructure, all of which are affected by real-world husbandry practices. The mechanisms are complex and underlie the wide range of reported emission factors for GHG and NH_3 (Hristov et al., 2011; Montes et al., 2013). At the sub-facility level, distinct emissions are expected from a range of farm structures and infrastructure including milking parlors and barns, corrals, manure piles, and fertilized crop fields, and for wet waste management, lagoons and slurry tanks (Owen and Silver, 2015). These activities and processes lead to different ratios of emitted trace gases.

The Chino dataset provided insights into identifying the fingerprints of differing and similar dairy practices between dairies and at the sub-facility scale. For example, plume β_7 for the individual dairy featured the highest R_E for CO_2/CH_4, contributing 30% of the dairy's CO_2, while only contributing just 14% of the dairy's NH_3 and a higher 23% of its CH_4. This would be consistent with an enteric emission source plus a natural gas combustion source, possibly with frequent waste material removal, such as at a milking barn, and/or suppression of NH_3 emissions by bedding material. The small plume β_6, which originated in a field, featured the lowest R_E for CO_2, and corresponded to between 5 and 22 cows, likely represents manure − either current or legacy. Dairies use such fields to spread manure for drying that creates strong CH_4 and NH_3 emission sources physically separate from the location of the cows.

Plume β_3 had the highest R_E for NH_3/CH_4 and interestingly its source may have been associated with a physical depression where water accumulated in a pond in several historical Google Earth images. A depression also likely indicates a location where subsurface water migration would transport NH_3 and NH_4 salts.

For dairy β the overall R_E for NH_3/CH_4 was 1.5, approximately triple the mean R_E for the Chino Dairy Complex, 0.42 ± 0.12, suggesting significantly different practices. In contrast, four different dairy plumes exhibited R_E values clustered within 1%, including the dominant plume P4, suggesting similar husbandry practices. The disagreement between dairy β and the overall dairy complex is easily understood in terms of magnitude − the plume from dairy β was only 0.8% of overall emissions.

4.7. Future directions

In this study, satellite NH_3 data provided seasonal variation information. One could then apply the emission factor ratio of CH_4 to NH_3 (approximately 2:1) to estimate exposure to CH_4. This same approach could be applied to gases with health implications, such as H_2S, to estimate exposure (Leifer et al., 2016b). Then, comparison with epidemiology studies can connect emissions and health impacts, providing suggestions for improved regulations. However, the data herein showed that this would be an oversimplification - the CH_4 emission seasonal variation was half that of NH_3 and not in phase. This certainly arises due to different processes associated with these gases' emissions, and similar process differences are very probable for H_2S and other trace husbandry gases. Thus, the seasonality of emission factors requires characterization.

Although important insights can be learned from animal chamber studies, they are reductionist and thus fail to capture the many aspects of real world dairy practices that vary from the ideal and are affected by multiple factors, including the differences between individual animals. Enteric emissions depend on the rumen microbial community structure, which is far more complicated than the human gut biome, and the importance to human health of the gut biome is only beginning to be understood. Due to rumen complexity and variability, studies seeking to modify the rumen microbiome to reduce emissions should have real-world dairy evaluation to identify emissions trade-offs between the target gas and other trace gases, which may have significant animal health and productivity and product quality implications.

This study shows how satellite remote sensing can be leveraged to improve regulation development through understanding processes that occur at the dairy and sub-dairy scale − a scale barely explored in this study. Ideally, repeat measurements should be collected that can resolve emissions at the sub-dairy scale contemporaneous with remote sensing data, in collaboration with dairy scientists to better understand the relationship to real world practices. Improved 3D wind measurements are needed to

characterize the effect of near field dispersion modification from structures. In this study, two gases (CH_4, NH_3) or three gases (adding CO_2) were used for fingerprinting plumes and to identify practices. The measurement of additional gases will provide additional information to aid plume fingerprinting.

All these criteria were achieved as part of on-going research efforts by repeat AMOG Surveyor data of emissions from the California Polytechnic State University research dairy including concurrent Mako observations. The Cal Poly Dairy includes two waste management lagoons, providing critical missing insights on typical intensive dairy practices — the near universal dry waste management of the Chino Dairy Complex is atypical and relates to its location in the middle of one of the largest urban centers of the US.

Most of the underlying mechanisms of seasonal variability remain unclear (beyond the temperature dependency of microbial trace gas production in waste), although they clearly are complex. Further investigation of the variability and its relationship to driving factors will provide insights into the likely impacts of climate change on husbandry emissions, particularly in light of the general industry trends towards increasing intensity in the US and globally, and increased husbandry product consumption in countries like India and China (Tilman et al., 2002), where NH_3 emissions are continuing to grow more rapidly than in the US. Increasing intensity provides greater mixing of feces and urea, a critical process in the production and emission of NH_3. Thus, husbandry CH_4 and NH_3 emissions are certain to play increasingly important roles in affecting the earth's radiative balance, particularly as they are likely to be amplified by positive feedbacks from increasing temperatures and changing rain patterns.

5. Conclusions

Mobile data were collected on 25 June 2015 for the Chino Dairy Complex, Los Angeles Basin in convoy fashion with AMOG Surveyor leading and recording *in situ* trace gas and meteorology measurements, and MISTIR making column measurements. Analyzed data were collected approximately orthogonal to the wind direction. Plume inversions were conducted on transects for the entire complex and for a single dairy. Inversions considered information from multiple gases and airborne trace gas remote sensing data collected by Mako. Analysis included long-term (9-yr.) satellite measurements by the Infrared Atmospheric Sounding Interferometer to derive seasonal variations. These observations showed clear downwind plumes that map out NH_3 and other husbandry trace gas exposures for downwind communities in this dense urban setting.

For the Chino Dairy Complex, agreement was within 5% between MISTIR and AMOG emissions: 15.7 versus 14.9, Gg NH_3 yr^{-1}, respectively when a multi-gas approach guided by the airborne remote sensing imagery was used. The remaining discrepancy most likely arose from higher turbulence due to structures in the semi-urban environment increasing the turbulence class by ~5%. Applying the NH_3-validated, informed transport model yielded CH_4 emissions of 30 Gg yr^{-1}. This was for 45,000 herd size, yielding emission factors at the high end of those reported.

Inversions for a single dairy were much less successful in terms of AMOG-MISTIR agreement, which was ~57% with MISTIR at 360 Gg NH_3 yr^{-1}. Underlying this was significant wind heterogeneity from downwind structures (convergence and divergence) and emissions unsteadiness in these near-field measurements. Estimated CH_4, NH_3, and CO_2 emissions were 91, 209, and 8200 Mg yr^{-1}, implying 2480, 1870, and 1720 head of cattle based on literature emission factors. Different plumes were connected to likely activities at source locations that included a structure with likely natural gas combustion (milking barn), manure storage, and cow sheds by trace gas fingerprints.

NH_3 downwind of the Chino Dairy Complex showed a seasonal variation of a factor of ten - a factor ~3 times larger than the literature suggests from variations in waste emissions and enteric emissions. This is proposed to result from the legacy soil emissions of a century of husbandry, supported by airborne remote sensing data showing widespread emissions from neighborhoods that had been dairies 15 years prior and AMOG and MISTIR observations of a broad associated plume. No emissions were observed from a similar neighborhood to the northwest that was not agricultural for at least many decades.

In addition, seasonal variations must be considered when comparing surveys in different seasons and provides insights into the implications of climate change.

In reviewing the literature of the biological mechanisms underlying seasonality in husbandry trace gas emissions, a number of important processes were identified relating in a broad sense to animal health. Given large emissions variability among replicate animals in chamber studies as well as variations among species and widely differing farm practices, farm-scale real world studies of husbandry emissions are more likely to produce relevant information and understanding than experiments carried out under highly controlled conditions.

Appendix B. Supplementary data

Supplementary data related to this article can be found at https://doi.org/10.1016/j.envpol.2018.03.078.

Table of Acronyms

AIRS	Atmospheric InfraRed Sounder
ANNI	Artificial Neural Network for IASI
AMOG	AutoMObile trace Gas Surveyor
CEAS	Cavity Enhanced Absorption Spectroscopy
CrIS	Cross-track Infrared Sounder
EDGAR	Emission Database for Global Atmospheric Research
FGGA	Fast Greenhouse Gas Analyzer
FTIR	Fourier Transform Infrared
GHG	Greenhouse Gas
GOSAT	Greenhouse gases Observing SATellite
GPS	Global Positioning System
IASI	Infrared Atmospheric Sounding Interferometer
LAX	Los Angeles Airport
LT	Local Time
MISTIR	Mobile Infrared Sensor for Tactical Incident Response
PBL	Planetary Boundary Layer
TES	Tropospheric Emission Spectrometer

TIR	Thermal Infrared
VOC	Volatile Organic Compounds

Table of Variables

A (−)	Stickiness parameter − 0 or 1
C (ppb)	Concentration
C' (ppb)	Concentration anomaly
D (km)	Distance to plume source
E (Gg yr^{-1})	Emissions
E_{AMOG} (Gg yr^{-1})	Emissions from AMOG data
E_{MISTIR} (Gg yr^{-1})	Emissions from MISTIR data
h (m)	Plume origin height
k (−)	Orographic forcing factor on Gaussian plume
PI (−)	Plume I in the Chino Dairy Complex plume model. For I = 1−8
R_E (−)	Trace gas emissions ratio of ammonia to methane
T (°C)	Temperature
u (m/s)	Wind speed
x (m)	Along wind direction
XC' (ppb-m)	Column concentration anomaly
y (m)	Crosswind direction
z (m)	Vertical direction
σ_x (m)	Turbulence parameter in x direction, also Gaussian plume half-width
σ_y (m)	Turbulence parameter in y direction
σ_z (m)	Turbulence parameter in z direction
β_I (−)	Plume I in the plumes model for dairy β. For I = 1 to 7

References

Amon, B., Amon, T., Boxberger, J., Alt, C., 2001. Emissions of NH_3, N_2O and CH_4 from dairy cows housed in a farmyard manure tying stall (housing, manure storage, manure spreading). Nutrient Cycl. Agroecosyst. 60, 103–113. https://doi.org/10.1023/A:1012649028772.

Andriamanohiarisoamanana, F.J., Sakamoto, Y., Yamashiro, T., Yasui, S., Iwasaki, M., Ihara, I., Nishida, T., Umetsu, K., 2017. The seasonal effects of manure management and feeding strategies on hydrogen sulphide emissions from stored dairy manure. J. Mater. Cycles Waste Manag. 19, 1253–1260. https://doi.org/10.1007/s10163-016-0519-7.

Aneja, V.P., Chauhan, J.P., Walker, J.T., 2000. Characterization of atmospheric ammonia emissions from swine waste storage and treatment lagoons. J. Geophys. Res.: Atmosphere 105, 11535–11545. https://doi.org/10.1029/2000JD900066.

Baek, B.H., Aneja, V.P., Tong, Q., 2004. Chemical coupling between ammonia, acid gases, and fine particles. Environ. Pollut. 129, 89–98. https://doi.org/10.1016/j.envpol.2003.09.022.

Bougouin, A., Leytem, A., Dijkstra, J., Dungan, R.S., Kebreab, E., 2016. Nutritional and environmental effects on ammonia emissions from dairy cattle housing: a meta-analysis. J. Environ. Qual. 45, 1123–1132. https://doi.org/10.2134/jeq2015.07.0389.

Braam, C.R., Ketelaars, J.J.M.H., Smits, M.C.J., 1997. Effects of floor design and floor cleaning on ammonia emission from cubicle houses for dairy cows. Neth. J. Agric. Sci. 45, 49–64. http://edepot.wur.nl/41774.

Briggs, G.A., 1973. Diffusion estimation for small emissions, atmospheric turbulence and diffusion laboratory, NOAA, ATDL contribution file. NOAA, air Resources atmospheric turbulence and diffusion laboratory, oak ridge. Tennessee 87–147.

Broucek, J., 2015. Methane yield from cattle, sheep, and goats housing with emphasis on emission factors: a review. Slovak Journal of Animal Science 48, 122–139. http://www.cvzv.sk/slju/15_3/5_Broucek.pdf.

Buckland, K., Young, S.J., Keim, E.R., Johnson, B.R., Johnson, P.D., Tratt, D.M., 2017. Tracking and quantification of gaseous chemical plumes from anthropogenic emission sources within the Los Angeles Basin. Rem. Sens. Environ. 201, 275–296. https://doi.org/10.1016/j.rse.2017.09.012.

Bussink, D.W., Oenema, O., 1998. Ammonia volatilization from dairy farming systems in temperate areas: a review. Nutrient Cycl. Agroecosyst. 51, 19–33. https://doi.org/10.1023/A:1009747109538.

Carslaw, D.C., Rhys-Tyler, G., 2013. New insights from comprehensive on-road measurements of NO_X, NO_2 and NH_3 from vehicle emission remote sensing in London, UK. Atmos. Environ. 81, 339–347. https://doi.org/10.1016/j.atmosenv.2013.09.026.

Casey, K.D., Bicudo, J.R., Schmidt, D.R., Singh, A., Gay, S.W., Gates, R.S., Jacobson, L.D., Hoff, S.J., 2006. Air quality and emissions from livestock and poultry production/Waste management systems. In: Rice, J.M., Caldwell, D.F., Humenik, F.J. (Eds.), Animal Agriculture and the Environment: National Center for Manure

and Animal Waste Management White Papers. American Society of Agricultural and Biological Engineers, St. Joseph, Michigan, pp. 1–40. https://doi.org/10.13031/2013.20246.

CDFA, 2002-2017. Dairy stats: Bi-Annual and annual summaries. Accessed: Mar. 2018. https://www.cdfa.ca.gov/dairy/dairystats_annual.html.

Chanton, J., Liptay, K., 2000. Seasonal variation in methane oxidation in a landfill cover soil as determined by an in situ stable isotope technique. Global Biogeochem. Cycles 14, 51–60. https://doi.org/10.1029/1999GB900087.

Clarisse, L., Clerbaux, C., Dentener, F., Hurtmans, D., Coheur, P.-F., 2009. Global ammonia distribution derived from infrared satellite observations. Nat. Geosci. 2, 479–483. https://doi.org/10.1038/NGEO551.

Clauss, M., Hume, I.D., Hummel, J., 2010. Evolutionary adaptations of ruminants and their potential relevance for modern production systems. Animal 4, 979–992. https://doi.org/10.1017/S1751731110000388.

Clerbaux, C., Boynard, A., Clarisse, L., George, M., Hadji-Lazaro, J., Herbin, H., Hurtmans, D., Pommier, M., Razavi, A., Turquety, S., Wespes, C., Coheur, P.-F., 2009. Monitoring of atmospheric composition using the thermal infrared IASI/MetOp sounder. Atmos. Chem. Phys. 9, 6041–6054. https://doi.org/10.5194/acp-9-6041-2009.

Conley, S., Faloona, I., Mehrotra, S., Suard, M., Lenschow, D.H., Sweeney, C., Herndon, S., Schwietzke, S., Pétron, G., Pifer, J., Kort, E.A., Schnell, R., 2017. Application of Gauss's theorem to quantify localized surface emissions from airborne measurements of wind and trace gases. Atmospheric Measurement Techniques 10, 3345–3358. https://doi.org/10.5194/amt-10-3345-2017.

Conley, S., Franco, G., Faloona, I., Blake, D.R., Peischl, J., Ryerson, T.B., 2016. Methane emissions from the 2015 Aliso canyon blowout in Los Angeles, CA. Science 351, 1317–1320. https://doi.org/10.1126/science.aaf2348.

Cottle, D.J., Nolan, J.V., Wiedemann, S.G., 2011. Ruminant enteric methane mitigation: a review. Anim. Prod. Sci. 51, 491–514. https://doi.org/10.1071/AN10163.

Dammers, E., Shephard, M.W., Palm, M., Cady-Pereira, K., Capps, S., Lutsch, E., Strong, K., Hannigan, J.W., Ortega, I., Toon, G.C., Stremme, W., Grutter, M., Jones, N., Smale, D., Siemons, J., Hrpcek, K., Tremblay, D., Schaap, M., Notholt, J., Erisman, J.W., 2017. Validation of the CrIS fast physical NH_3 retrieval with ground-based FTIR. Atmospheric Measurement Techniques 10, 2645–2667. https://doi.org/10.5194/amt-10-2645-2017.

Dawson, J.P., Adams, P.J., Pandis, S.N., 2007. Sensitivity of PM2.5 to climate in the Eastern US: a modeling case study. Atmos. Chem. Phys. 7, 4295–4309. https://doi.org/10.5194/acp-7-4295-2007.

Edinger, J.G., 1959. Changes in the depth of the marine layer over the Los Angeles Basin. J. Meteorol. 16, 219–226. doi: 10.1175/1520-0469(1959)016<0219:citdot>2.0.co;2

Ellis, J.L., Bannink, A., France, J., Kebreab, E., Dijkstra, J., 2010. Evaluation of enteric methane prediction equations for dairy cows used in whole farm models. Global Change Biol. 16, 3246–3256. https://doi.org/10.1111/j.1365-2486.2010.02188.x.

Ellis, J.L., Kebreab, E., Odongo, N.E., Beauchemin, K., McGinn, S., Nkrumah, J.D., Moore, S.S., Christopherson, R., Murdoch, G.K., McBride, B.W., Okine, E.K., France, J., 2009. Modeling methane production from beef cattle using linear and nonlinear approaches. J. Anim. Sci. 87, 1334–1345. https://doi.org/10.2527/jas.2007-0725.

EPA, 2017. In: Mausami, D., Weitz, M. (Eds.), 2017 Inventory of US Greenhouse Gas: Emissions and Sinks: 1990-2015. Environmental Protection Agency, Washington DC, p. 633.

European Commission, 2009. Emission database for global atmospheric research (EDGAR). http://edgar.jrc.ec.europa.eu.

European Commission, 2016. Emission database for global atmospheric research (EDGAR) version 4.3.1. http://edgar.jrc.ec.europa.eu.

FAO, 2016. FAOSTAT: Live animals. Accessed: Oct. 2016. http://www.fao.org/faostat/en/-data/QA.

Galloway, J.N., Townsend, A.R., Erisman, J.W., Bekunda, M., Cai, Z., Freney, J.R., Martinelli, L.A., Seitzinger, S.P., Sutton, M.A., 2008. Transformation of the nitrogen cycle: recent trends, questions, and potential solutions. Science 320, 889–892. https://doi.org/10.1126/science.1136674.

Garnsworthy, P.C., Craigon, J., Hernandez-Medrano, J.H., Saunders, N., 2012. Variation among individual dairy cows in methane measurements made on farm during milking. J. Dairy Sci. 95, 3181–3189. https://doi.org/10.3168/jds.2011-4606.

Gilliland, A.B., Dennis, R.L., Roselle, S.J., Pierce, T.E., 2003. Seasonal NH_3 emission estimates for the eastern United States based on ammonium wet concentrations and an inverse modeling method. J. Geophys. Res.: Atmosphere 108, 4477. https://doi.org/10.1029/2002jd003063.

Grainger, C., Clarke, T., McGinn, S.M., Auldist, M.J., Beauchemin, K.A., Hannah, M.C., Waghorn, G.C., Clark, H., Eckard, R.J., 2007. Methane emissions from dairy cows measured using the sulfur hexafluoride (SF_6) tracer and chamber techniques. J. Dairy Sci. 90, 2755–2766. https://doi.org/10.3168/jds.2006-697.

Gurjar, B.R., Butler, T.M., Lawrence, M.G., Lelieveld, J., 2008. Evaluation of emissions and air quality in megacities. Atmos. Environ. 42, 1593–1606. https://doi.org/10.1016/j.atmosenv.2007.10.048.

Hall, J.L., Boucher, R.H., Buckland, K.N., Gutierrez, D.J., Keim, E.R., Tratt, D.M., Warren, D.W., 2016. Mako airborne thermal infrared imaging spectrometer - performance update. In: Silny, J.F., Ientilucci, E.J. (Eds.), Imaging Spectromtery XXI. Society of Photo-optical Instrumentation Engineers (SPIE), p. 997604. San Diego, CA.

Hanna, S.R., Briggs, G.A., Hosker Jr., R.P., 1982. Handbook on Atmospheric Diffusion. Technical Information Center. U.S. Department of Energy, p. 110.

Harper, L.A., Flesch, T.K., Powell, J.M., Coblentz, W.K., Jokela, W.E., Martin, N.P., 2009. Ammonia emissions from dairy production in Wisconsin. J. Dairy Sci. 92, 2326–2337. https://doi.org/10.3168/jds.2008-1753.

Heald, C.L., Collett Jr., J.L., Lee, T., Benedict, K.B., Schwandner, F.M., Li, Y., Clarisse, L., Hurtmans, D.R., Van Damme, M., Clerbaux, C., Coheur, P.F., Philip, S., Martin, R.V., Pye, H.O.T., 2012. Atmospheric ammonia and particulate inorganic nitrogen over the United States. Atmos. Chem. Phys. 12, 10295–10312. https://doi.org/10.5194/acp-12-10295-2012.

Hertel, O., Reis, S., Skjoth, C.A., Bleeker, A., Harrison, R., Cape, J.N., Fowler, D., Skiba, U., Simpson, D., Jickells, T., 2011. Nitrogen processes in the atmosphere. In: Sutton, M.A., Howard, C.M., Erisman, J.W., Billen, G., Bleeker, A., Grennfelt, P., van Grinsven, H., Grizzetti, B. (Eds.), The European Nitrogen Assessment: Sources, Effects and Policy Perspectives. Cambridge University Press, Cambridge, UK, pp. 177–207. http://nora.nerc.ac.uk/id/eprint/14575.

Howarth, R.W., 2008. Estimating atmospheric nitrogen deposition in the Northeastern United States: relevance to Narragansett Bay. In: Desbonnet, A., Costa-Pierce, B.A. (Eds.), Science for Ecosystem-based Management. Springer, New York, pp. 47–65. https://doi.org/10.1007/978-0-387-35299-2_3.

Hristov, A.N., Hanigan, M., Cole, A., Todd, R., McAllister, T.A., Ndegwa, P.M., Rotz, A., 2011. Review: ammonia emissions from dairy farms and beef feedlots. Can. J. Anim. Sci. 91, 1–35. https://doi.org/10.4141/cjas10034.

Hristov, A.N., Ott, T., Tricarico, J., Rotz, A., Waghorn, G., Adesogan, A., Dijkstra, J., Montes, F., Oh, J., Kebreab, E., Oosting, S.J., Gerber, P.J., Henderson, B., Makkar, H.P.S., Firkins, J.L., 2013. SPECIAL TOPICS — mitigation of methane and nitrous oxide emissions from animal operations: III. A review of animal management mitigation options. J. Anim. Sci. 91, 5045–5069. https://doi.org/10.2527/jas.2013-6585.

IPCC, 2013. Working Group 1 contribution to the IPCC fifth assessment report climate change 2013-the physical science basis. In: Stocker, T., Dahe, Q., Plattner, G.-K. (Eds.), International Panel on Climate Change. IPCC Secretariat, Geneva, Switzerland, p. 2216.

Kinsman, R., Sauer, F.D., Jackson, H.A., Wolynetz, M.S., 1995. Methane and carbon dioxide emissions from dairy cows in full lactation monitored over a six-month period. J. Dairy Sci. 78, 2760–2766. https://doi.org/10.3168/jds.S0022-0302(95)76907-7.

Kong, Y., Xia, Y., Seviour, R., Forster, R., McAllister, T.A., 2013. Biodiversity and composition of methanogenic populations in the rumen of cows fed alfalfa hay or triticale straw. FEMS (Fed. Eur. Microbiol. Soc.) Microbiol. Ecol. 84, 302–315. https://doi.org/10.1111/1574-6941.12062.

Krautwurst, S., Gerilowski, K., Kolyer, R.W., Jonsson, H., Krings, T., Horstjann, M., Leifer, I., Vigil, S., Buchwitz, M., Schuettemeyer, D., Fladeland, M.M., Burrows, J.P., Bovensmann, H., 2016. Detected methane emissions from landfills in the Los Angeles Basin during the COMEX campaign by the Methane Airborne MAPper (MAMAP) instrument and an airborne greenhouse gas in-situ analyzer. Atmos. Chem. Phys. 10, 3429–3452. https://doi.org/10.5194/amt-10-3429-201.

Kuze, A., Suto, H., Nakajima, M., Hamazaki, T., 2009. Thermal and near infrared sensor for carbon observation Fourier-transform spectrometer on the Greenhouse Gases Observing Satellite for greenhouse gases monitoring. Appl. Optic. 48, 6716–6733. https://doi.org/10.1364/AO.48.006716.

Leen, J.B., Yu, X.Y., Gupta, M., Baer, D.S., Hubbe, J.M., Kluzek, C.D., Tomlinson, J.M., Hubbell 2nd, M.R., 2013. Fast in situ airborne measurement of ammonia using a mid-infrared off-axis ICOS spectrometer. Environ. Sci. Technol. 47, 10446–10453. https://doi.org/10.1021/es401134u.

Leifer, I., Culling, D., Schneising, O., Farrell, P., Buchwitz, M., Burrows, J., 2013. Transcontinental methane measurements: Part 2. Mobile surface investigation of fossil fuel industrial fugitive emissions. Atmos. Environ. 74, 432–441. https://doi.org/10.1016/j.atmosenv.2013.03.018.

Leifer, I., Melton, C., Fischer, M.L., Fladeland, M., Frash, J., Gore, W., Iraci, L.T., Marrero, J., Ryoo, J.-M., Tanaka, T., Yates, E., 2018. Atmospheric characterization through fused mobile airborne and surface *in situ* surveys: methane emissions quantification from a producing oil field. Atmospheric Measurement Techniques 11, 1689–1705. https://doi.org/10.5194/amt-11-1689-2018.

Leifer, I., Melton, C., Frash, J., Fischer, M.L., Cui, X., Murray, J.J., Green, D.S., 2016a. Fusion of mobile in situ and satellite remote sensing observations of chemical release emissions to improve disaster response. Front. Sci. 4, 1–14. https://doi.org/10.3389/fenvs.2016.00059.

Leifer, I., Melton, C., Manish, G., Leen, B., 2014. Mobile monitoring of methane leakage. Gases and Instrumentation July/August 2014, 20–24. http://www.lgrinc.com/publications/Mobile%20Monitoring%20of%20Methane%20Leakage.pdf.

Leifer, I., Melton, C., Tratt, D.M., Buckland, K.N., Clarisse, L., Coheur, P., Frash, J., Gupta, M.X., Johnson, P.D., Leen, B., van Damme, M., Whitburn, S., Yurganov, L., 2016b. Remote sensing and in situ measurements of methane and ammonia emissions from a megacity dairy complex: Chino, CA. Environ. Pollut. 221, 37–51. https://doi.org/10.1016/j.envpol.2016.09.083.

Leifer, I., Melton, C., Tratt, D.M., Frash, J., Manish, G.X., Leen, B., Buckland, K.N., Johnson, P.D., 2016c. Comparing imaging spectroscopy and in situ observations of Chino Dairy Complex emissions. In: Chanussot, J. (Ed.), 8th Workshop on Hyperspectral Image and Signal Processing: Evolution in Remote Sensing. IEEE, Los Angeles, CA.

Leytem, A.B., Dungan, R.S., Bjorneberg, D.L., Koehn, A.C., 2011. Emissions of ammonia, methane, carbon dioxide, and nitrous oxide from dairy cattle housing and manure management systems. J. Environ. Qual. 40, 1383–1394. https://doi.org/10.2134/jeq2009.0515.

Lu, R., Turco, R.P., Jacobson, M.Z., 1997. An integrated air pollution modeling system for urban and regional scales: 1. Structure and performance. J. Geophys. Res.: Atmosphere 102, 6063–6079. https://doi.org/10.1029/96jd03501.

McGinn, S.M., Flesch, T.K., Harper, L.A., Beauchemin, K.A., 2006. An approach for measuring methane emissions from whole farms. J. Environ. Qual. 35, 14–20. https://doi.org/10.2134/jeq2005.0250.

MESONET, 2017. ASOS-AWOS-METAR data download. https://mesonet.agron.iastate.edu/request/download.phtml?network=CA_ASOS.

Misselbrook, T.H., Powell, J.M., 2005. Influence of bedding material on ammonia emissions from cattle excreta. J. Dairy Sci. 88, 4304–4312. https://doi.org/10.3168/jds.S0022-0302(05)73116-7.

Montes, F., Meinen, R., Dell, C., Rotz, A., Hristov, A.N., Oh, J., Waghorn, G., Gerber, P.J., Henderson, B., Makkar, H.P.S., Dijkstra, J., 2013. SPECIAL TOPICS — mitigation of methane and nitrous oxide emissions from animal operations: II. A review of manure management mitigation options 1. J. Anim. Sci. 91, 5070–5094. https://doi.org/10.2527/jas.2013-6584.

Ngwabie, N.M., Jeppsson, K.H., Gustafsson, G., Nimmermark, S., 2011. Effects of animal activity and air temperature on methane and ammonia emissions from a naturally ventilated building for dairy cows. Atmos. Environ. 45, 6760–6768. https://doi.org/10.1016/j.atmosenv.2011.08.027.

Nowak, J.B., Neuman, J.A., Bahreini, R., Middlebrook, A.M., Holloway, J.S., McKeen, S.A., Parrish, D.D., Ryerson, T.B., Trainer, M., 2012. Ammonia sources in the California South Coast Air Basin and their impact on ammonium nitrate formation. Geophys. Res. Lett. 39, L07804. https://doi.org/10.1029/2012gl051197.

Owen, J.J., Silver, W.L., 2015. Greenhouse gas emissions from dairy manure management: a review of field-based studies. Global Change Biol. 21, 550–565. https://doi.org/10.1111/gcb.12687.

Paulot, F., Jacob, D.J., 2014. Hidden cost of U.S. agricultural exports: particulate matter from ammonia emissions. Environ. Sci. Technol. 48, 903–908. https://doi.org/10.1021/es4034793.

Paulot, F., Jacob, D.J., Johnson, M.T., Bell, T.G., Baker, A.R., Keene, W.C., Lima, I.D., Doney, S.C., Stock, C.A., 2015. Global oceanic emission of ammonia: constraints from seawater and atmospheric observations. Global Biogeochem. Cycles 29, 1165–1178. https://doi.org/10.1002/2015GB005106.

Paulot, F., Jacob, D.J., Pinder, R.W., Bash, J.O., Travis, K., Henze, D.K., 2014. Ammonia emissions in the United States, European Union, and China derived by high-resolution inversion of ammonium wet deposition data: interpretation with a new agricultural emissions inventory (MASAGE_NH3). J. Geophys. Res.: Atmosphere 119, 4343–4364. https://doi.org/10.1002/2013JD021130.

Peischl, J., Ryerson, T.B., Brioude, J., Aikin, K.C., Andrews, A.E., Atlas, E., Blake, D., Daube, B.C., de Gouw, J.A., Dlugokencky, E., Frost, G.J., Gentner, D.R., Gilman, J.B., Goldstein, A.H., Harley, R.A., Holloway, J.S., Kofler, J., Kuster, W.C., Lang, P.M., Novelli, P.C., Santoni, G.W., Trainer, M., Wofsy, S.C., Parrish, D.D., 2013. Quantifying sources of methane using light alkanes in the Los Angeles basin, California. J. Geophys. Res.: Atmosphere 118, 4974–4990. https://doi.org/10.1002/jgrd.50413.

Peterson, N.G., 2000. The Future of the Chino Milk Shed in the Los Angeles Basin, 30th California Alfalfa Symposium and 29th National Alfalfa Symposium. University of California, Davis, Las Vegas, Nevada, p. 5.

Phillips, V.R., Scholtens, R., Lee, D.S., Garland, J.A., Sneath, R.W., 2000. A review of methods for measuring emission rates of ammonia from livestock buildings and slurry or manure stores, part 1: assessment of basic approaches. J. Agric. Eng. Res. 77, 355–364. https://doi.org/10.1006/jaer.2000.0613.

Pinder, R.W., Gilliland, A.B., Dennis, R.L., 2008. Environmental impact of atmospheric NH₃ emissions under present and future conditions in the eastern United States. Geophys. Res. Lett. 35, L12808. https://doi.org/10.1029/2008gl033732.

Powell, J.M., Broderick, G.A., Misselbrook, T.H., 2008. Seasonal diet affects ammonia emissions from tie-stall dairy barns. J. Dairy Sci. 91, 857–869. https://doi.org/10.3168/jds.2007-0588.

Reynolds, C.K., Kristensen, N.B., 2008. Nitrogen recycling through the gut and the nitrogen economy of ruminants: an asynchronous symbiosis. J. Anim. Sci. 86, E293–E305. https://doi.org/10.2527/jas.2007-0475.

Saint-Pierre, B., Wright, A.-D.G., 2012. Diversity of gut methanogens in herbivorous animals. Animal 7, 49–56. https://doi.org/10.1017/S1751731112000912.

Sarkwa, F.O., Timpong-Jones, E.C., Assuming-Bediako, N., Aikins, S., Adogla-Bessa, T., 2016. The contribution of livestock production to climate change: a review. Livest. Res. Rural Dev. 28 (37). http://www.lrrd.org/lrrd28/3/sark28037.htm.

Sasakawa, M., Shimoyama, K., Machida, T., Tsuda, N., Suto, H., Arshinov, M., Davydov, D., Fofonov, A., Krasnov, O., Saeki, T., Koyama, Y., Maksyutov, S., 2010. Continuous measurements of methane from a tower network over Siberia. Tellus B 62, 403–416. https://doi.org/10.1111/j.1600-0889.2010.00494.x.

Schiffman, S.S., Bennett, J.L., Raymer, J.H., 2001. Quantification of odors and odorants from swine operations in North Carolina. Agric. For. Meteorol. 108, 213–240. https://doi.org/10.1016/S0168-1923(01)00239-8.

Shephard, M.W., Cady-Pereira, K.E., Luo, M., Henze, D.K., Pinder, R.W., Walker, J.T., Rinsland, C.P., Bash, J.O., Zhu, L., Payne, V.H., Clarisse, L., 2011. TES ammonia retrieval strategy and global observations of the spatial and seasonal variability of ammonia. Atmos. Chem. Phys. 11, 10743–10763. https://doi.org/10.5194/acp-11-10743-2011.

Sherlock, R.R., Sommer, S.G., Khan, R.Z., Wood, C.W., Guertal, E.A., Freney, J.R., Dawson, C.O., Cameron, K.C., 2002. Ammonia, methane, and nitrous oxide emission from pig slurry applied to a pasture in New Zealand. J. Environ. Qual. 31, 1491–1501. https://doi.org/10.2134/jeq2002.1491.

Sommer, S.G., Hutchings, N.J., 2001. Ammonia emission from field applied manure

and its reduction. Eur. J. Agron. 15, 1–15. https://doi.org/10.1016/S1161-0301(01)00112-5.

Stelson, A.W., Seinfeld, J.H., 1982. Relative humidity and temperature dependence of the ammonium nitrate dissociation constant. Atmos. Environ. 16, 983–992. https://doi.org/10.1016/0004-6981(82)90184-6.

Sutton, M.A., Reis, S., Riddick, S.N., Dragosits, U., Nemitz, E., Theobald, M.R., Tang, Y.S., Braban, C.F., Vieno, M., Dore, A.J., Mitchell, R.F., Wanless, S., Daunt, F., Fowler, D., Blackall, T.D., Milford, C., Flechard, C.R., Loubet, B., Massad, R., Cellier, P., Personne, E., Coheur, P.F., Clarisse, L., Van Damme, M., Ngadi, Y., Clerbaux, C., Skjøth, C.A., Geels, C., Hertel, O., Wichink Kruit, R.J., Pinder, R.W., Bash, J.O., Walker, J.T., Simpson, D., Horváth, L., Misselbrook, T.H., Bleeker, A., Dentener, F., de Vries, W., 2013. Towards a climate-dependent paradigm of ammonia emission and deposition. Phil. Trans. Biol. Sci. 368, 20130166. https://doi.org/10.1098/rstb.2013.0166.

Thompson, D., Leifer, I., Bovensman, H., Eastwood, M., Fladeland, M., Frankenberg, C., Gerilowski, K., Green, R., Krautwurst, S., Krings, T., Luna, B., Thorpe, A.K., 2015. Real-time remote detection and measurement for airborne imaging spectroscopy: a case study with methane. Atmospheric Measurement Techniques 8, 1–46. https://doi.org/10.5194/amtd-8-1-2015.

Tilman, D., Cassman, K.G., Matson, P.A., Naylor, R., Polasky, S., 2002. Agricultural sustainability and intensive production practices. Nature 418, 671. https://doi.org/10.1038/nature01014.

Tratt, D.M., Young, S.J., Lynch, D.K., Buckland, K.N., Johnson, P.D., Hall, J.L., Westberg, K.R., Polak, M.L., Kasper, B.P., Qian, J., 2011. Remotely sensed ammonia emission from fumarolic vents associated with a hydrothermally active fault in the Salton Sea Geothermal Field, California. J. Geophys. Res.: Atmosphere 116, D21308. https://doi.org/10.1029/2011jd016282.

Van Damme, M., Clarisse, L., Heald, C.L., Hurtmans, D., Ngadi, Y., Clerbaux, C., Dolman, A.J., Erisman, J.W., Coheur, P.F., 2014. Global distributions, time series and error characterization of atmospheric ammonia (NH$_3$) from IASI satellite observations. Atmos. Chem. Phys. 14, 2905–2922. https://doi.org/10.5194/acp-14-2905-2014.

Van Damme, M., Whitburn, S., Clarisse, L., Clerbaux, C., Hurtmans, D., Coheur, P.-F., 2017. Version 2 of the IASI NH$_3$ neural network retrieval algorithm: near-real time and reanalysed datasets. Atmospheric Measurement Techniques 2017,

4905–4914. https://doi.org/10.5194/amt-10-4905-2017.

Viatte, C., Lauvaux, T., Hedelius, J.K., Parker, H., Chen, J., Jones, T., Franklin, J.E., Deng, A.J., Gaudet, B., Verhulst, K., Duren, R., Wunch, D., Roehl, C., Dubey, M.K., Wofsy, S., Wennberg, P.O., 2017. Methane emissions from dairies in the Los Angeles basin. Atmos. Chem. Phys. 17, 7509–7528. https://doi.org/10.5194/acp-17-7509-2017.

Warner, J.X., Wei, Z., Strow, L.L., Dickerson, R.R., Nowak, J.B., 2016. The global tropospheric ammonia distribution as seen in the 13-year AIRS measurement record. Atmos. Chem. Phys. 16, 5467–5479. https://doi.org/10.5194/acp-16-5467-2016.

Wennberg, P.O., Mui, W., Wunch, D., Kort, E.A., Blake, D.R., Atlas, E.L., Santoni, G.W., Wofsy, S.C., Diskin, G.S., Jeong, S., Fischer, M.L., 2012. On the sources of methane to the Los Angeles atmosphere. Environ. Sci. Technol. 46, 9282–9289. https://doi.org/10.1021/es301138y.

Wescott, P., Trostle, R., 2007. USDA Agricultural Projections to 2023. Office of the Chief Economist, World Agricultural Outlook Board. U.S. Department of Agriculture, p. 97.

Whitburn, S., Van Damme, M., Clarisse, L., Bauduin, S., Heald, C.L., Hadji-Lazaro, J., Hurtmans, D., Zondlo, M.A., Clerbaux, C., Coheur, P.-F., 2016. A flexible and robust neural network IASI-NH$_3$ retrieval algorithm. J. Geophys. Res.: Atmosphere 121, 6581–6599. https://doi.org/10.1002/2016JD024828.

White, W.H., Anderson, J.A., Blumenthal, D.L., Husar, R.B., Gillani, N.V., Husar, J.D., Wilson, W.E., 1976. Formation and transport of secondary air pollutants: ozone and aerosols in the St. Louis urban plume. Science 194, 187–189. https://doi.org/10.1126/science.959846.

Wikipedia, 2007. Geography of California. Accessed: Oct. 2017. https://en.wikipedia.org/wiki/Geography_of_California-/media/File:California_Topography-MEDIUM.png.

Wu, Y.-J., Wang, Y., Qian, D., 2007. A Google-map-based Arterial Traffic Information System, IEEE Intelligent Transportation Systems Conference (ITSC). Institute of Electrical and Electronic Engineers, Bellevue, WA, pp. 968–973.

Young, S.J., 2002. Detection and Quantification of Gases in Industrial-stack Plumes Using Thermal Infrared Hyperspectral Imaging. Aerospace Corporation, El Segundo, CA, p. 76.